IMPROVING THE CALCULATION OF THE SENSITIVITY CURVE AND FREQUENCY ARRANGEMENT OF THE SCHENBERG GW DETECTOR

Arthur Pereira dos Reis

Master's Dissertation of the Graduate Course in Astrophysics, guided by Drs. Odylio Denys de Aguiar, and Rubens de Melo Marinho Junior, approved in June 17, 2021.

INPE

São José dos Campos

2021

IMPROVING THE CALCULATION OF THE SENSITIVITY CURVE AND FREQUENCY ARRANGEMENT OF THE SCHENBERG GW DETECTOR

Arthur Pereira dos Reis

Master's Dissertation of the Graduate Course in Astrophysics, guided by Drs. Odylio Denys de Aguiar, and Rubens de Melo Marinho Junior, approved in June 17, 2021.

URL of the original document:
<http://urlib.net/8JMKD3MGP3W34T/44TS9CL>

INPE

São José dos Campos

2021

INSTITUTO NACIONAL DE PESQUISAS ESPACIAIS
Serviço de Pós-Graduação - SEPGR

DEFESA FINAL DE DISSERTAÇÃO DE ARTHUR PEREIRA DOS REIS
BANCA Nº 175/2021, REG 296969/2019

No dia 17 de junho de 2021, as 14 horas, por teleconferência, o(a) aluno(a) mencionado(a) acima defendeu seu trabalho final (apresentação oral seguida de arguição) perante uma Banca Examinadora, cujos membros estão listados abaixo. O(A) aluno(a) foi APROVADO(A) pela Banca Examinadora, por unanimidade, em cumprimento ao requisito exigido para obtenção do Título de Mestre em Astrofísica. O trabalho precisa da incorporação das correções sugeridas pela Banca Examinadora e revisão final pelo(s) orientador(es).

Título: "Improving the calculation of the sensitivity curve and frequency arrangement of the Schenberg GW Detector"

Observações da banca: A banca enviará ao candidato e orientadores as sugestões e correções ao texto e os orientadores serão responsáveis pela verificação final do texto da dissertação.

Eu, Carlos Alexandre Wuensche de Souza, Presidente da Banca Examinadora, assino esta ATA, em nome de todos os membros, com o consentimento dos mesmos.

Dr. Carlos Alexandre Wuensche de Souza - Presidente - INPE
Dr. Odylio Denys de Aguiar - Orientador - INPE
Dr. Rubens de Melo Marinho Jr - Orientador - ITA/IEF
Dr. Massimo Tinto - Membro Interno - INPE
Dr. Fabio da Silva Bortoli - Membro Externo - IFSP
Dr. César Henrique Lenzi - Membro Externo - ITA/IEF

Referência: Processo nº 01340.003873/2021-19   SEI nº 7601330

ACKNOWLEDGEMENTS

ABSTRACT

Gravitational Wave (GW) Astronomy is maturing into an integral part of multi-messenger astronomy as, to this date, 50 events have been detected, including some with observed counterparts. However, until now all were measured by the same technique of ground based interferometry. The Brazilian Gravitational Wave Detector Mario Schenberg, a resonant mass antenna whose project started in 2000, has the prospect of contributing to the advancement of the field by providing an additional way to observe gravitational radiation. The antenna was disassembled and relocated after the last engineering run and another upgrade is being considered. In the meantime, work is being done with what is now known about GWs and this detector. This work contributes to this effort by providing an investigation of the behavior that is seen in the frequencies of the resonant mass' quadrupole modes. Here are shown results from FEM simulations of deformed models and heterogeneous models of the antenna. These could be possible explanations for a known anomaly in the frequency structure of the detector. Additionally, a mathematical model of calculating the sensitivity curve of the instrument is presented. A new estimate for the curve is shown with data gathered during the preparation of this work.

Palavras-chave: Gravitational Waves. Detector. Finite Element Methods. Vibration modes.

APRIMORAMENTO DO CÁLCULO DA CURVA DE SENSIBILIDADE E ARRANJO DAS FREQUÊNCIAS DO DETECTOR DE OG SCHENBERG

RESUMO

A Astronomia de Ondas Gravitacionais (OG) vêm se estabelecendo como parte importante da astronomia multi-mensageira visto que, até hoje, 50 eventos foram detectados, incluindo alguns cujas contrapartes foram observadas. Entretanto, até agora todos foram medidos pela única técnica de interferometria em solo. O detector de Ondas Gravitacionais brasileiro Mario Schenberg, uma antena de massa ressonante cujo projeto começou em 2000, tem a possibilidade de contribuir para o avanço desse campo por possibilitar uma maneira adicional de se observar a radiação gravitacional. A antena foi desmontada e realocada após a última corrida de engenharia e mais uma modernização vem sendo considerada. No meio tempo, trabalhos estão sendo realizados com o que já se sabe sobre OGs e sobre esse detector. Essa obra contribui com esse esforço ao providenciar uma investigação do comportamento que é visto nas frequências dos modos quadupolares da massa ressonante. Aqui serão mostrados resultados de simulações de MEF de modelos deformados e modelos heterogêneos da antena. Estas poderiam ser possíveis explicações para uma anomalia identificada nos arranjos de frequência do detector. Adicionalmente, um modelo matemático para se calcular a curva de sensibilidade do instrumento é mostrado. Uma nova estimativa para a curva é mostrada a partir de dados coletados durante a realização deste trabalho.

Palavras-chave: Gravitational Waves. Detector. Finite Element Methods. Vibration modes.

LIST OF FIGURES

LIST OF TABLES

Page

xiii

CONTENTS

1 INTRODUCTION

The field of Gravitational Wave (GW) Astronomy is a novelty no more. Six years have already passed from the first detection of gravitational waves (ABBOTT et al., 2016) and 50 events have been detected until now. So far, all sources of gravitational radiation were from binary coalescences of compact objects and the catalog contains detections of types BH-BH (Black Hole - Black Hole), BH-NS (Black Hole - Neutron Star) and NS-NS. Direct evidence was found for previously unobserved compact objects such as an intermediate mass black holes and the candidate for the heaviest known neutron star. Therefore, GW astronomy has already established a foothold as a way to study astrophysical objects. Furthermore, it is also being used as a way to evaluate GR and alternative theories of gravitation (FERREIRA, 2019; ALBERT et al., 2019).

It is in this scenario that the Mario Schenberg Gravitational Wave Antenna currently exists in. The Schenberg is a Brazilian cryogenic spherical resonant mass GW detector of the latest generation, developed in parallel of its "sister" antenna from the Netherlands, the MiniGRAIL. The project officially started in 2000 and so far had a number of engineering runs, with upgrades on several of its systems in between. In theory, this detector has a project strain sensitivity of $h \sim 10^{-22}/\sqrt{\text{Hz}}$ at $3.2\,\text{kHz}$ (TOBAR et al., 2000; AGUIAR et al., 2002; AGUIAR et al., 2004; AGUIAR et al., 2008; AGUIAR et al., 2012; OLIVEIRA; AGUIAR, 2016). So far, this experiment has reached a sensitivity of $h \sim 10^{-20}/\sqrt{\text{Hz}}$ in its last run, but have not yet detected gravitational waves (OLIVEIRA; AGUIAR, 2016).

Matter of fact, all detections so far were made by ground based interferometers (LIGO and VIRGO). Schenberg, which is supposed to be the state-of-the-art for resonant mass detectors, was surpassed by one of aLIGO's interferometers during its O3 run, with a strain sensitivity $h \sim 10^{-22}/\sqrt{\text{Hz}}$ around $3kHz$ (BUIKEMA et al., 2020)).

Given this and considering that reaching maximum available performance will require the research and development of a multitude of technologies and techniques, it is possible to become skeptic in relation to this project. To evaluate how much this effort is worth, there is a work in progress that tries to estimate how many, if any, of the events detected by the O2 and O3 runs of the LIGO-VIRGO collaboration would also be registered in an updated Schenberg's readout (AGUIAR, 2021).

But to either match or surpass the capabilities of the current network of ground-

based laser interferometers, a resonant mass observatory would require a collection of antennas of different sizes (commonly called a "xylophone" arrangement) each with their respective instrumentation and while also improving upon the current state-of-the-art.

Although the situation seems dire, there are plenty of reasons to keep working in this field. The most important aspect, perhaps, is the convergence of evidence that a detection by something else than a ground based interferometer would bring upon science. Since they don't share the same idiosyncrasies and should be affected only by independent systematic errors, a simultaneous and matching observation by different techniques would strengthen our confidence in both (SCHICKORE, 2018). If, however, the nature of the signal measured by this other detector differs from the interferometers', it would suggest that either our understanding of the theory behind GW detection is lacking or a new physics is needed. And since LISA's, a space-base interferometer, launch date is more than a decade away; and with the SKA, a radiotelescope capable of using a pulsar timing array, also years away, it becomes apparent that, being the best candidate of its class of resonant mass detectors, Schenberg has the real possibility of being the second type of instrument capable of directly measure gravitational radiation, after only ground based interferometers.

And the second point to be made is that such challenge motivates the advancement of the several associated technologies that are part of Schenberg's systems. For instance, the development of parametric transducers of high electric and mechanical quality factors; constructing a chamber capable of reaching high vacuum while providing vibration isolation and interfacing with the cryogenics; ways of acquiring and processing data; and so on. The cryogenic system deserves special consideration, since the operational antenna will probably be the heaviest known object to be kept at $< 1\,\mathrm{K}$.

Lastly, the full scope of the resonant mass technique is not yet totally explored. There is a recent proposal to use the Moon as a natural GW antenna (HARMS et al., 2021). Perhaps the insights gained here from the lab scale will prove fruitful for those other projects.

The antenna is currently out of commission, after being moved out of the Low Temperature Laboratory at the University of São Paulo (LESBT/IFUSP) and into the National Institute for Space Research (INPE) after the run of 2015. It was not yet assembled, as data from the last run is analyzed and a system upgrade is being taken into consideration and developed.

In this work, I present an exploration of the behaviors of the quadrupole modes of vibration and discuss possible explanations for a yet not explained experimental result. Finally, with data gathered during the writing of this volume, I include an updated version of the sensitivity curve.

2 GRAVITATIONAL WAVES

Although the discussion over the idea that gravity could have a finite speed of propagation predates Einstein, it was his theory of General Relativity (GR) from 1915 that first introduced the concept of gravitational waves as we know today (CERVANTES-COTA et al., 2016). At first, GWs were considered just an artifact of the mathematical framework of the theory, as the wave equation was found to be a valid solution of the field equations but with no other physical meaning. This chapter will bring an overview of the mathematical framework around GWs and some properties of this object. Latter on the next chapter this will be used to describe how radiation interacts with matter and how it can be measured.

2.1 Linearized gravity

The first step to obtain the gravitational wave equation is to consider the Einstein Field Equations (MAGGIORE, 2008):

$$R_{\mu\nu} - \frac{1}{2}Rg_{\mu\nu} = \frac{8\pi G}{c^4}T_{\mu\nu} = G_{\mu\nu} \tag{2.1}$$

They comprise 10 non-linear coupled differential equations, that are remarkably difficult to solve. Analytical solutions are generally produced considering special cases, while Numerical Relativity deals with other situations, if sufficient computational power exists. So, following the spirit of the first approach, some assumptions will be made to simplify this problem.

The goal here is just to show the existence of a valid wave-like solution for the field equations on the most simple scenario: flat space, away from any distribution of mass and energy. At the moment, there is no consideration about the mechanism of gravitational wave generation. Also, without any effects of propagation through cosmological scales.

The metric $g_{\mu\nu}$ that describes a local spacetime where a small perturbation occurs on top of a flat spacetime can be written as:

$$g_{\mu\nu} = \eta_{\mu\nu} + h_{\mu\nu} \tag{2.2}$$

Where $\eta_{\mu\nu} = \text{diag}[-1, 1, 1, 1]$ is the Minkowski metric and $|h_{\mu\nu}| \ll 1$ is perturbative term. Using this to write the connection, its terms consisting of derivatives of the

Minkowski will vanish. The terms that remain are:

$$\Gamma^{\mu}_{\nu\rho} = \frac{1}{2}\eta^{\mu\sigma}(h_{\sigma\rho,\nu} + h_{\sigma\nu,\rho} - h_{\nu\rho,\sigma}) \tag{2.3}$$

With the connection, it is now possible to write the Riemman tensor. Also, let's already suppress terms of order $\mathcal{O}(h^2)$ and above.

$$R_{\mu\nu\rho\sigma} = \frac{1}{2}\left(\partial_\nu\partial_\rho h_{\mu\sigma} + \partial_\mu\partial_\sigma h_{\nu\rho} - \partial_\nu\partial_\sigma h_{\mu\rho} - \partial_\mu\partial_\rho h_{\nu\sigma}\right) \tag{2.4}$$

Contract it with $\eta^{\mu\rho}$ to get Ricci's tensor:

$$R_{\nu\sigma} = \frac{1}{2}\left(\partial_\nu\partial_\rho h^\rho{}_\sigma + \partial^\rho\partial_\sigma h_{\nu\rho} - \partial_\nu\partial_\sigma h - \partial^\rho\partial_\rho h_{\nu\sigma}\right) \tag{2.5}$$

And analogously, the Ricci scalar:

$$R = \partial^\nu\partial_\rho h^\rho{}_\nu - \partial^\rho\partial_\rho h \tag{2.6}$$

Substituting (2.5) and (2.6) into (2.1) we arrive at an expression for the Einstein tensor depending on the derivatives of the perturbative part of the metric:

$$G_{\nu\sigma} = R_{\nu\sigma} - \frac{1}{2}\eta_{\nu\sigma}R$$
$$G_{\nu\sigma} = \frac{1}{2}\left(\partial_\nu\partial_\rho h^\rho{}_\sigma + \partial^\rho\partial_\sigma h_{\nu\rho} - \partial_\nu\partial_\sigma h - \partial^\rho\partial_\rho h_{\nu\sigma} - \eta_{\nu\sigma}\partial^\mu\partial_\rho h^\rho{}_\mu + \eta_{\nu\sigma}\partial^\rho\partial_\rho h\right) \tag{2.7}$$

The equations of motion that follows from this are at linearly dependent of h and its derivatives, with no terms of higher orders, hence why it's called a linearized theory.

To rewrite this expression in a more fashionable manner, it is possible to substitute $h^{\mu\nu}$ by another metric function $\overline{h}^{\mu\nu}$ defined as

$$\overline{h}^{\mu\nu} = h^{\mu\nu} - \frac{1}{2}\eta^{\mu\nu}h \tag{2.8}$$

easy to verify that

$$\overline{h} = -h \tag{2.9}$$

which will then allow the Equation (2.7) to be written as

$$G_{\nu\sigma} = -\frac{1}{2}\left(\partial^\rho\partial_\rho \overline{h}_{\nu\sigma} + \eta_{\nu\sigma}\partial^\mu\partial_\rho \overline{h}^\rho{}_\mu - 2\partial_\nu\partial^\rho \overline{h}_{\rho\sigma}\right) \tag{2.10}$$

It is possible to arrive at an even more compact form. Since no assumption was made about the choice of gauge yet, there is the freedom to choose $\overline{h}$ so $\partial^\beta \overline{h}_{\alpha\beta} = 0$, which is called Lorentz or De Donder gauge. The mathematical justification for this freedom can be found in Maggiore (2008). This choice reduces our degrees of freedom from 10 to 6.

In this gauge, the field Equations (2.10) become:

$$G_{\mu\nu} = -\frac{1}{2}\partial^\rho\partial_\rho\overline{h}_{\mu\nu}$$

or using the d'Alambertian operator notation $\square^2 = \partial^\rho\partial_\rho$

$$G_{\mu\nu} = -\frac{1}{2}\square^2\overline{h}_{\mu\nu} = \frac{8\pi G}{c^4}T_{\mu\nu}$$

and therefore

$$\square^2\overline{h}_{\mu\nu} = -\frac{16\pi G}{c^4}T_{\mu\nu} \tag{2.11}$$

As stated in the beginning, it is going to be considered a situation far from mass and energy distributions, where $T_{\mu\nu} = 0$. So

$$\square^2\overline{h}_{\mu\nu} = 0 \tag{2.12}$$

Furthermore, when outside a source, $\partial^\beta \overline{h}_{\alpha\beta} = 0$ can become invariant, depending on the chosen coordinate transformation. Let a transformation of type

$$x_\mu \to x'_\mu = x_\mu + \xi_\mu \tag{2.13}$$

chosen so that $\square^2\xi_\mu = 0$. Thus, by the definition of tensor transformation,

$$h_{\mu\nu} \to h'_{\mu\nu} = h_{\mu\nu} - (\partial_\nu\xi_\mu + \partial_\mu\xi_\nu), \tag{2.14}$$

assuming $\partial\xi$ is at most of the same order of h. Additionally, lets' say that ξ satisfies:

$$\square^2\xi_{\mu\nu} = \partial_\mu\xi_\nu + \partial_\nu\xi_\mu - \eta_{\mu\nu}\partial^\rho\xi_\rho = 0 \tag{2.15}$$

So, under transformation, h will be

$$\overline{h}_{\mu\nu} \to \overline{h}'_{\mu\nu} = \overline{h}_{\mu\nu} - (\partial_\nu\xi_\mu + \partial_\mu\xi_\nu - \eta_{\mu\nu}\partial_\rho\xi^\rho) \tag{2.16}$$

And the derivative will contain:

$$\partial^\nu \overline{h}_{\mu\nu} \to \partial^\nu \overline{h}'_{\mu\nu} = \partial^\nu \overline{h}_{\mu\nu} - \Box^2 \xi_\mu \tag{2.17}$$

Therefore, depending on the choice of ξ, this is invariant.

When the trace is chosen to be zero $\overline{h}^\rho{}_\rho = \overline{h} = 0$ the consequence is that $\overline{h} = h$ and the bar can be dropped from here on now. Also, the static part is gone $\partial^0 h_{00} = h_{00} = 0$. Lastly, the remaining time cross components are zero $h^{0i} = 0$. This plus de Donder gauge is the transverse-traceless gauge (noted as TT).

In this gauge we can write the d'Alambertian in a more explicit and very familiar form:

$$\Box^2 h_{\mu\nu}^{TT} = -\frac{1}{c^2}\partial_0^2 h_{ij}^{TT} + \nabla^2 h_{ij}^{TT} = 0 \tag{2.18}$$

Which is a wave equation. In the next section a solution will be provided and some of its properties will be examined.

2.2   Wave equation

Let's assume that the metric perturbation tensor $h_{\mu\nu}$ will be projected to the TT gauge and a coordinate system will be chosen such that $\hat{\mathbf{z}}$ coincides with direction of propagation, meaning $k^i = k\hat{\mathbf{z}}$. Also, consider a plane normal to $\hat{\mathbf{n}} = (0, 0, 0, k/\omega)$, therefore parallel to the propagation.

In the TT gauge, Equation (2.18) has a plane wave solution of form

$$h_{ij}^{TT}(x) = e_{ij}(\mathbf{k})e^{ikx} \tag{2.19}$$

where e_{ij} is the polarization tensor and the wave vector is $k^\mu = (\omega/c, 0, 0, k)$, or in the matricial form:

$$h_{ij}^{TT}(t, z) = \begin{pmatrix} h_{xx} & h_{xy} & 0 \\ h_{yx} & -h_{yy} & 0 \\ 0 & 0 & 0 \end{pmatrix} \tag{2.20}$$

Since h is traceless, $h_{xx} + h_{yy} = 0$, and since it is symmetric, $h_{xy} = h_{yx}$, so

$$h_{ij}^{TT}(t, z) = \begin{pmatrix} h_+ & h_\times & 0 \\ h_\times & -h_+ & 0 \\ 0 & 0 & 0 \end{pmatrix} e^{-i\omega(t-z/c)} \tag{2.21}$$

This is the equation of a planar wave, propagating along $\hat{\mathbf{z}}$, tensorial in nature and

8

with 2 polarizations (h_+ and $h_\times$).

To get the TT gauge from an arbitrary system, we'll use a projection operation. Let us define the following tensor,

$$P_{ij}(\hat{\mathbf{n}}) = \delta_{ij} - n_i n_j \tag{2.22}$$

that is symmetric and transverse ($n^i P_{ij}(\hat{\mathbf{n}}) = n^i \delta_{ij} - n^i n_i n_j = 0$) with trace $P_{ii} = 2$. This tensor acts as a project operator: $P_{ij} P_{jk} = P_{ik}$. Now, defining another tensor:

$$\Lambda_{ij,kl}(\hat{\mathbf{n}}) = P_{ik} P_{jl} - \frac{1}{2} P_{ij} P_{kl} \tag{2.23}$$

$$\Lambda_{ij,kl}(\hat{\mathbf{n}}) = \delta_{ik}\delta_{jl} - \frac{1}{2}\delta_{ij}\delta_{kl} - n_j n_l \delta_{ik} - n_i n_k \delta_{jl}$$
$$+ \frac{1}{2} n_k n_l \delta_{ij} + \frac{1}{2} n_i n_j \delta_{kl} + \frac{1}{2} n_i n_j n_k n_l \tag{2.24}$$

It is symmetric, if considering simultaneous exchange $i \Longleftrightarrow j$, $k \Longleftrightarrow l$. It is transverse to all indices ($n^i \Lambda_{ij,kl} = n^j \Lambda_{ij,kl} = n^k \Lambda_{ij,kl} = n^l \Lambda_{ij,kl} = 0$) and traceless $\Lambda_{ii,kl} = \Lambda_{ij,kk} = 0$.

Now, the transverse traceless gauge can be obtained by projecting any given h (MAGGIORE, 2008):

$$h_{ij}^{TT} = \Lambda_{ij,kl} h_{kl} \tag{2.25}$$

The use of this gauge allows to easily construct the equations of plane-waves with the classical separation of time and spatial coordinates to denote propagation.

2.2.1 Wave generation

It is natural to reach for inspiration in another classical field theory that has already a well-developed framework in order to study the generation and propagation of waves. And there are plenty of parallels between gravitational waves and its electromagnetic counterpart.

Here, we'll use the method of finding a suitable Green's function that solves a differential equation with boundary conditions, as commonly done in electrodynamics (JACKSON, 1999). Considering $\Box_x^2$ the d'Alambertian in respect to x , then If $G(x - x')$ satisfies

$$\Box_x^2 G(x - x') = \delta^4(x - x') \tag{2.26}$$

then it can be shown that eq. (2.11) has a solution (MAGGIORE, 2008)

$$\bar{h}_{\mu\nu}(t, x) = \frac{4G}{c^4} \int d^4x' G(x - x') T_{\mu\nu}(x') \tag{2.27}$$

Since this is a problem that involves the propagation of the causal effect of a source over a field, it is suitable to impose the boundary condition that G is a retarded Green function:

$$G(x - x') = \frac{1}{4\pi |\mathbf{x} - \mathbf{x}'|} \delta^4(ct - ct_{\text{ret}}) \tag{2.28}$$

where $t_{ret} = t - \frac{|\mathbf{x} - \mathbf{x}'|}{c}$ is the <u>retarded time</u>.

Substituting this into eq. (2.27), we'll arrive at:

$$\bar{h}_{\mu\nu}(t, \mathbf{x}) = \frac{4G}{c^4} \int d^3x' \frac{1}{|\mathbf{x} - \mathbf{x}'|} T_{\mu\nu}(t_{ret}, \mathbf{x}') \tag{2.29}$$

It is apparent in this equation that any change in the source term will mean a change in the metric field only after a finite amount of time.

Now, using (2.25) and projecting (2.29) into the TT gauge

$$h_{\mu\nu}^{TT}(t, \mathbf{x}) = \frac{4G}{c^4} \Lambda_{ij,kl}(\hat{\mathbf{n}}) \int d^3x' \frac{1}{|\mathbf{x} - \mathbf{x}'|} T_{\mu\nu}(t_{ret}, \mathbf{x}') \tag{2.30}$$

Comparing eq. 2.30 with the analogous solutions for the case of the electromagnetic field (JACKSON, 1999) their similarities will become evident:

$$\mathbf{E}(t, \mathbf{x}) = \frac{1}{4\pi\epsilon_0} \int d^3x' \frac{1}{|\mathbf{x} - \mathbf{x}'|} \left(-\nabla'\rho(t_{ret}, \mathbf{x}') - \frac{1}{c^2} \frac{\partial \mathbf{J}(t_{ret}, \mathbf{x}')}{\partial t'} \right) \tag{2.31}$$

$$\mathbf{B}(t, \mathbf{x}) = \frac{\mu_0}{4\pi} \int d^3x' \frac{1}{|\mathbf{x} - \mathbf{x}'|} (\nabla \times \mathbf{J}(t_{ret}, \mathbf{x}')) \tag{2.32}$$

In both cases, the equation relates a field to a source but imposes a finite speed of information propagation. Their main difference lies in the order of the tensors. Besides that, both fields magnitudes follow a $1/r^2$ relation in respect to the distance from the source.

In the case of electromagnetism, a change in charge density distribution will cause a variation on the field, and this variation propagates at c. In the case of gravitation, a change in mass density distribution (or energy-momentum, in the most general case) will cause a change in the spacetime curvature. And this information also propagates

at c.

But in the more specific case of what can generate a wave, there is a crucial difference. In EM, a dipole can exist, and a changing dipole (rotating, for example) will produce an alternating field that will propagate as a wave, which when far from the source can be simplified to the planar wave equation. More complex charge distributions, such as quadrupoles and beyond also will be accounted for.

Mass, however, doesn't form dipoles. There is no anti-mass, capable of creating repulsive gravity field, that will pair up with mass to form a dipole. There is even a justification involving the nature of the force carrier. A photon has helicity of ± 1, which has the implication of allowing the existence of dipoles. But gravitons have helicity ± 2, that allows quadrupoles.

An example of a distribution of mass that has a quadrupole moment is a binary system. There are two bodies with mass going around but always on opposing sides through their baricenter, always leaving a region of no mass that follows their trail.

The energy-momentum tensor components can be described by (MISNER et al., 1973)

$$T_{00} = (\rho + p)v_0 v_0 - p \tag{2.33a}$$

$$T_{0j} = T_{j0} = \rho v_j \tag{2.33b}$$

$$T_{ij} = \rho v_i v_j + p\delta_{ij} \tag{2.33c}$$

Now, considering a non-relativistic mass distribution, where the pressure component is insignificant compared to the rest mass terms:

$$T_{00} \approx \rho v_0 v_0 = \rho_0 c^2 + \rho_0 v^2/2 \tag{2.34a}$$

$$T_{ij} \approx \rho v_i v_j = \rho_0 c^2 + \rho_0 v_i v_j \tag{2.34b}$$

substituting it into Equation (2.29) will result in

$$h_{ij}(t, \mathbf{x}) = \frac{2G}{rc^4} \frac{\partial^2}{\partial t^2} \int \rho x_i x_j \mathrm{d}^3 x \tag{2.35}$$

Consider the expression for the quadrupole moment of a mass distribution:

$$I_{ij} = \int \rho x_i x_j \mathrm{d}^3 x \tag{2.36}$$

11

Lets define the reduced quadrupole moment as

$$I_{ij} = \int T_{00}(x_i x_j - \delta_{ij} x_k^2) \, \mathrm{d}^3 x \tag{2.37}$$

To write it in the TT gauge, we use the Lambda tensor

$$I_{ij}^{TT} = \Lambda_{ij,kl} I_{kl} \tag{2.38}$$

$$\tag{2.39}$$

to arrive at

$$I_{ij}^{TT} = P_{il} P_{jm} I_{lm} - \frac{1}{2} P_{ij} P_{lm} I_{lm} \tag{2.40}$$

using (2.36) and (2.34) and comparing with (2.35)

$$h_{ij}(t, \mathbf{x}) = \frac{2G}{rc^4} \ddot{I}_{ij}^{TT}(t_{\mathrm{ret}}, \mathbf{x}') \tag{2.41}$$

Finally, this last equation provides a relation between perturbation and source. Of course, the exact waveform properties such as the power spectral density and polarization will be dependent on the nature of the source. For some cases, binaries during the inspiral, for example, there are Post Newtonian approximations that were capable of generating templates of gravitational waves. However, for the most complex systems, for instance the merger of those same objects, it becomes necessary to use Numerical Relativity to calculate the waveform. In Schenberg's case, the sources of interest, i.e. the ones that lies inside its band, are mostly the coalescence of low-mass compact object binaries. So far no burst-like signal has ever been detected, so the jury is still out on neutron starquakes and other astrophysical events that could be detected by the antenna.

2.2.2 Interaction with matter

In General Relativity, any particle follows a trajectory in spacetime called its world line. The behavior of this path depends on the metric of the spacetime in which this curve is inscribed. Something that effects the metric will, consequentially, also act upon the dynamics of the particle.

As we're interested in studying how a detector would work, that means that we are interested in the weak field regimen, far from any source. In this situation, an

expression for effective force density can be found in Ashby e Dreitlein (1975) and is as follows:

$$f_i^{GW} = \frac{1}{2}\rho\frac{\partial^2 h_{ij}}{\partial t^2}x_j \tag{2.42}$$

In the following chapter this equation will be used to describe how a resonant mass detector can respond to a gravitational wave.

2.3 Spherical amplitudes

In this section, the tensor $h_{\mu\nu}$ will be rewritten in a form that will be useful later. First, consider that force in Equation (2.42) is defined as a gradient of a scalar potential ϕ:

$$f_i^{GW} = \nabla_i\Phi(\mathbf{x}, t) \tag{2.43}$$

and comparing with the equation that relates it with h_{ij}:

$$\nabla_i\Phi(\mathbf{x}, t) = \nabla_i\left(\frac{1}{4}\rho\frac{\partial^2 h_{jk}}{\partial t^2}x_j x_k\right)$$

$$\phi(\mathbf{x}, t) = \frac{1}{4}\rho\frac{\partial^2 h_{ij}}{\partial t^2}x_i x_j \tag{2.44}$$

Now, we'll use the spherical harmonics to form a basis and write the potential as a combination of this basis (MERKOWITZ, 1995). Consider the real spherical harmonics Y_{2m}, as these form an orthonormal basis. And let the five spherical amplitudes h_m, $m = 1, \ldots 5$ be such that

$$\ddot{h}_{ij}x_i x_j = \sqrt{\frac{2\pi}{15}}r^2\ddot{h}_m(t)Y_{2m}(\theta, \phi) \tag{2.45}$$

Finally, its only necessary to write an expression that relates the wave equation written in the frame of the lab to the more convenient notation of the spherical amplitudes. So, the following matrix transforms the components h_+ and $h_\times$ of the wave into these five spherical amplitudes:

$$\begin{pmatrix} h_1(t) \\ h_2(t) \\ h_3(t) \\ h_4(t) \\ h_5(t) \end{pmatrix} = \begin{pmatrix} \frac{1}{2}(1 + \cos^2\beta)\cos 2\gamma & \cos\beta\sin 2\gamma \\ -\frac{1}{2}(1 + \cos^2\beta)\sin 2\gamma & \cos\beta\cos 2\gamma \\ -\frac{1}{2}\sin 2\beta\sin\gamma & \sin\beta\cos\gamma \\ \frac{1}{2}\sin 2\beta\cos\gamma & \sin\beta\sin\gamma \\ \frac{\sqrt{3}}{2}\sin^2\beta & 0 \end{pmatrix} \cdot \begin{pmatrix} h_+(t) \\ h_\times(t) \end{pmatrix} \tag{2.46}$$

Where β and γ are the polar and azimuthal angles in the detector's frame, respec-

tively.

3 RESONANT MASS GRAVITATIONAL WAVE DETECTORS

During the decades following GR's publication, arguments were thrown back and forth and in the 1950s a consensus was being reached that GWs were in fact a physical phenomenon. The discussion then shifted towards which observables would be produced and how they would be detected. Weber proposed and built the first detector during the 1960s (WEBER, 1960). It was a bar-shaped resonant mass detector that was supposed to, but failed to, directly detect gravitational waves.

The observation of radio signals from the now known as Hulse-Taylor pulsar in 1974 was the 1st indirect evidence for GW. The source of the signal was a binary system of a neutron star and a pulsar, which emitted periodic pulses with great regularity, effectively allowing to track their orbital period with astonishing precision. This allowed to observe an orbital decay that strongly agreed with GR's prediction of generation of gravitational wave radiation (HULSE; TAYLOR, 1975).

After this results, the following decades experienced a rush to detect GWs directly. Most of the effort was concentrated in two types of detectors: resonant mass antennas and ground based interferometers. Both had since many generations and iterations, in which their technology was constantly upgraded.

The resonant mass detectors started out as cylindrical bars, kept at room temperature, with a belt of piezoelectric gauges to detect its strain. At the present moment, these detectors use a different, more capable, geometry and have much more sensitive ways to detect the vibrations of the antenna.

In this chapter I'll present the theory behind resonant mass detectors, starting with a general overview and going up to the specific case of a spherical body.

3.1 Sphere eigenfunctions

The basis of the theoretical framework behind the resonant mass detectors starts with the theory of small, linear vibrations in elastic bodies. For a body of an arbitrary geometry, defined as mass distribution $\rho(\mathbf{x})$, Young's modulus E and Poisson's ratio ν, let $\mathbf{u}(\mathbf{x})$ be the displacement on the surface. For small amplitudes, the equations of motion for an elastic body driven by a force density $\mathbf{f}$ is (LANDAU, 1981):

$$\rho\ddot{\mathbf{u}} - \mu\nabla^2\mathbf{u} - (\lambda + \mu)\boldsymbol{\nabla}(\boldsymbol{\nabla}\cdot\mathbf{u}) = \mathbf{f}(\mathbf{x}, t) \tag{3.1}$$

Where λ, μ are the Lamé coefficients, defined as

$$\lambda = \frac{\nu E}{(1+\nu)(1-2\nu)}; \tag{3.2a}$$

$$\mu = \frac{E}{2(1+\nu)} \tag{3.2b}$$

Since here we are considering the interaction of the gravitational wave with the body, the force density is given by (2.42). Therefore,

$$\rho \ddot{u}_i - \mu \nabla^2 u_i - (\lambda + \mu)\boldsymbol{\nabla}(\boldsymbol{\nabla} \cdot u_i) = \frac{1}{2}\rho \frac{\partial^2 h_{ij}}{\partial t^2} x_j \tag{3.3}$$

Until now, no assumptions were made about the nature of the body. But in order to find a fashionable solution to these equations, from here onward some considerations will be taken. First, the geometry of the detector of interest is based on a sphere. So, to proceed, we'll find the solutions of the unforced case for a spherical body.

$$\rho \ddot{\mathbf{u}} - \mu \nabla^2 \mathbf{u} - (\lambda + \mu)\boldsymbol{\nabla}(\boldsymbol{\nabla} \cdot \mathbf{u}) = 0 \tag{3.4}$$

For such spherical body, the displacement can be written as a separation of a time dependent and spatial dependent parts (MERKOWITZ; JOHNSON, 1995):

$$\mathbf{u}(\mathbf{x}, t) = \sum_m a_m(t)\boldsymbol{\Psi}_m(\mathbf{x}) \tag{3.5}$$

where the index m indicates the different modes. So each mode of vibration will have a different associated amplitude a_m. The spatial part $\boldsymbol{\Psi}_m$ is defined as the solution of (3.1) in the case of a free, unforced sphere:

$$\rho \ddot{\mathbf{u}} - \mu \nabla^2 \mathbf{u} - (\lambda + \mu)\boldsymbol{\nabla}(\boldsymbol{\nabla} \cdot \mathbf{u}) = 0$$

$$\rho \sum_m \ddot{a}_m \boldsymbol{\Psi}_m - \mu \sum_m a_m \nabla^2 \boldsymbol{\Psi}_m - (\lambda + \mu)\sum_m a_m \boldsymbol{\nabla}(\boldsymbol{\nabla} \cdot \boldsymbol{\Psi}_m) = 0$$

$$-\omega^2 \rho \sum_m a_m \boldsymbol{\Psi}_m - \mu \sum_m a_m \nabla^2 \boldsymbol{\Psi}_m - (\lambda + \mu)\sum_m a_m \boldsymbol{\nabla}(\boldsymbol{\nabla} \cdot \boldsymbol{\Psi}_m) = 0$$

assume each ψ_m is solution of

$$-\omega^2 \rho \boldsymbol{\Psi}_m - \mu \nabla^2 \boldsymbol{\Psi}_m - (\lambda + \mu)\boldsymbol{\nabla}(\boldsymbol{\nabla} \cdot \boldsymbol{\Psi}_m) = 0 \tag{3.6}$$

Where ω is the frequency of resonance. At first let's assume that the system is degenerate, latter on the solution will include the non-degenerate case with ω_m. The spatial component Ψ will define which regions of the body suffers more or less of the

displacement for a given mode, the temporal component a_m comprises the oscillation of that mode. For this system of m equations, the eigenfunction Ψ_m of a sphere can be written in terms of the spherical harmonics Y_m (MERKOWITZ, 1995):

$$\boldsymbol{\Psi}_{lm}(r,\theta,\phi) = [\alpha_l(r)\hat{\mathbf{r}} + \beta_l(r)R\boldsymbol{\nabla}]Y_{lm}(\theta,\phi) \tag{3.7}$$

in this work, only interested in l = 2, so Psi is defined as

$$\boldsymbol{\Psi}_m(r,\theta,\phi) = [\alpha_2(r)\hat{\mathbf{r}} + \beta_2(r)R\boldsymbol{\nabla}]Y_{2m}(\theta,\phi) \tag{3.8}$$

When $l = 2$ these are called the quadrupole modes. And they are of interest as they are the only ones excited by gravitational radiation[1], if GR is the correct theory of gravitational. In Figure 3.1 a visualization of the five quadrupole modes is presented. The condition of normalization must also be satisfied:

$$\int_V \boldsymbol{\Psi}_m(\mathbf{x}) \cdot \boldsymbol{\Psi}_n(\mathbf{x})\,\mathrm{d}^3x = N_m\delta_{mn} \tag{3.9}$$

And the terms α, β in Equation (3.8) are called the radial eigenfunctions. They are as follows:

$$\alpha(r) = p_1 R\frac{\partial j_2(qr)}{\partial r} + 6p_2\frac{R}{r}j_2(kr) \tag{3.10a}$$

$$\beta(r) = p_1 j_2(qr) + 6p_2\frac{\partial r j_2(kr)}{\partial qr} \tag{3.10b}$$

The function j_2 is the Bessel function of order two, that is written as

$$j_l(x) = \left(\frac{1}{x}\frac{\mathrm{d}}{\mathrm{d}x}\right)^l\left(\frac{\sin x}{x}\right) \tag{3.11a}$$

$$j_2(x) = \left(\frac{3}{x^3} - \frac{1}{x}\right)\sin x - \frac{3\cos x}{x^2} \tag{3.11b}$$

while the coefficients k and q are defined as:

$$q^2 = \rho\frac{\omega_0^2}{\lambda + 2\mu} \tag{3.12a}$$

$$k^2 = \rho\frac{\omega_0^2}{\mu} \tag{3.12b}$$

---

[1]Caveat: the prolate-oblate mode, Y_{20}, is not excited directly.

Where ω_0 is the frequency in the case of the of the degenerate system. Finally, the coefficients p_1 and p_2 are such that the following boundary condition is satisfied:

$$p_1 \frac{\mathrm{d}}{\mathrm{d}r}\left(\frac{j_2(qr)}{r}\right) + p_2\left(\frac{5}{r^2} - \frac{k^2}{2} - \frac{1}{2}\frac{\mathrm{d}}{\mathrm{d}r}\right)j_2(kr) = 0 \qquad (3.13\mathrm{a})$$

$$p_1\left(\frac{6}{r^2} - \frac{k^2}{2} - \frac{2}{r}\frac{\mathrm{d}}{\mathrm{d}r}\right)j_2(qr) + 6p_2\frac{\mathrm{d}}{\mathrm{d}r}\left(\frac{j_2(kr)}{r}\right) = 0 \qquad (3.13\mathrm{b})$$

Figure 3.1 - Composition showing a representation of each of the 5 quadrupole modes of the sphere. These images were created from a FEM simulation of a homogeneous solid sphere. Each element is a superposition of two frames, half a period apart, so it captures the instants of maximum deformation. The color scale indicates the amplitude of deformation in respect to the body at rest; blue and red means zero and maximum deformation respectively. From left to right, $m = -2, -1, \ldots, 2$.
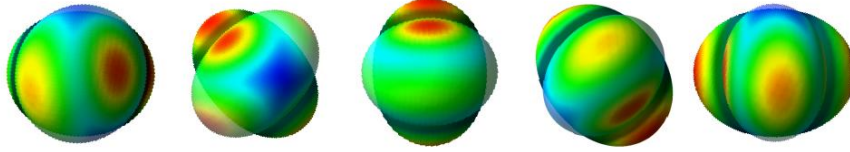
SOURCE: From the author.

3.2 Effective force

In this section we will formulate how the interaction mentioned in Section 2.2.2 will relate to the force acting upon an elastic body. From Equation (3.5), given that the limit of small vibration is being considered, it is possible to assume that the time component is of type

$$a_m(t) = A_m \exp(i\omega_m t) \qquad (3.14)$$

so

$$\ddot{a}_m = -\omega_m^2 a_m \qquad (3.15)$$

If substituted back into the forced condition Equation (3.1):

$$\rho\ddot{\mathbf{u}} - \mu\nabla^2\mathbf{u} - (\lambda + \mu)\boldsymbol{\nabla}(\boldsymbol{\nabla}\cdot\mathbf{u}) = \mathbf{f}(\mathbf{x}, t) \tag{3.16}$$

$$\rho\sum_m \ddot{a}_m\boldsymbol{\Psi}_m - \mu\sum_m a_m\nabla^2\boldsymbol{\Psi}_m - (\lambda + \mu)\sum_m a_m\boldsymbol{\nabla}(\boldsymbol{\nabla}\cdot\boldsymbol{\Psi}_m) = \mathbf{f}$$

using the result of Eq. (3.6)

$$\rho\sum_m \ddot{a}_m\boldsymbol{\Psi}_m - \sum_m a_m\underbrace{\left(\mu\nabla^2\boldsymbol{\Psi}_m + (\lambda + \mu)\boldsymbol{\nabla}(\boldsymbol{\nabla}\cdot\boldsymbol{\Psi}_m)\right)}_{-\rho\omega_m^2\boldsymbol{\Psi}_m} = \mathbf{f}$$

$$\rho\sum_m (\ddot{a}_m + \omega_m^2 a_m)\boldsymbol{\Psi}_m = \mathbf{f} \tag{3.17}$$

now multiplying $\boldsymbol{\Psi}_n$ and integrating in d^3x

$$\rho\sum_m (\ddot{a}_m + \omega_m^2 a_m)\int_V \boldsymbol{\Psi}_m\cdot\boldsymbol{\Psi}_n\,\mathrm{d}^3x = \int_V \mathbf{f}\cdot\boldsymbol{\Psi}_n\,\mathrm{d}^3x \tag{3.18}$$

using the normalization condition (3.9)

$$\ddot{a}_m + \omega_m^2 a_m = \frac{1}{\rho N}\int_V \mathbf{f}\cdot\boldsymbol{\Psi}_m\,\mathrm{d}^3x \tag{3.19}$$

And without loss of generality, it's possible to add a damping term

$$\ddot{a}_m + \frac{1}{\tau}\dot{a}_m + \omega_m^2 a_m = \frac{1}{\rho N}\int_V \mathbf{f}\cdot\boldsymbol{\Psi}_m\,\mathrm{d}^3x \tag{3.20}$$

From Equation (3.19), one can see that the effective force of a gravitational wave that is exciting the m-th mode of a body is:

$$F_m^{\mathrm{eff}} \equiv \int_V \mathbf{f}^{\mathrm{GW}}\cdot\boldsymbol{\Psi}_m\,\mathrm{d}^3x \tag{3.21}$$

It is now possible to compare it to the expression for force density (2.42) and $\boldsymbol{\Psi}_m$ (3.8). Furthermore, using (2.45) to write in spherical harmonics basis we finally arrive at

$$F_m^{\mathrm{eff}}(t) = \sqrt{\frac{4\pi}{15}}\rho\ddot{h}_m(t)R^4[p_1 j_2(qR) + 3P_2 j_2(kR)] \tag{3.22}$$

19

or

$$F_m^{\text{eff}}(t) = \frac{1}{2}\ddot{h}_m m_S \chi R \tag{3.23}$$

Where m_S is the mass of the sphere and χ is a coupling factor depending on the Poisson's ratio (MERKOWITZ, 1995). Which will be handy expressions to relate the effective force, as will appear in the equations of motion, with the passing gravitational wave.

3.3 Equations of motion

Equation (3.5) describes the displacement of the surface of the sphere, and latter on expressions that relate it to the spherical harmonics have been shown. Unfortunately, describing the motion of the points on the sphere is not enough for our purposes, as it is necessary to describe also what happens with the coupled resonators as well. There are already well-developed techniques for solving N coupled oscillators with small deviations from equilibrium – as would be this case (GOLDSTEIN, 1980).

3.3.1 Linear systems of differential equations

From here on now, the following notation will be adopted. Double underscore to represent matrices, $\underline{\underline{A}}$, and single underscore, vectors, $\underline{v}$. We try to write the equations of motion in a matricial form of type similar to

$$\underline{\underline{T}}\ddot{\underline{\eta}} + \underline{\underline{V}}\underline{\eta} = 0 \tag{3.24}$$

for which the solution is guessed to be

$$\underline{\eta} = C\underline{a}e^{-i\omega t} \tag{3.25}$$

Substituting this solution into (3.24)

$$-\omega^2 \underline{\underline{T}}\,\underline{a} + \underline{\underline{V}}\,\underline{a} = 0 \tag{3.26}$$

Here lie N coupled linear equations, that only can have non-trivial solution if its determinant vanishes

$$\det\left(-\omega^2 \underline{\underline{T}} + \underline{\underline{V}}\right) = 0 \tag{3.27}$$

Furthermore, it is possible to apply a change of coordinates $\underline{\eta} \to \underline{\eta}'$ so that $\underline{\underline{T}} \to \underline{\underline{\delta}}$.

Also, calling $\omega^2 = \lambda$ we'll read

$$\underline{V}\underline{a} = \lambda\underline{a} \tag{3.28}$$

It is known that finding the eigenvalues and eigenvectors of this equation is a way of solving the original system of equations. And without loss of generality, a more general solution that would also be including a complex part could also be used. Of course, the solution that describes the motion involves only the real part.

$$\eta_i = a_{ik}(C_k^+ e^{+i\omega_k t} + C_k^- e^{-i\omega_k t}) \tag{3.29}$$

3.3.2 Model matrix

Now back to the original problem, there are j transducers, each with 2 resonators, coupled to the surface of the vibrating sphere. Let $\hat{\mathbf{r}}_j$ be radial vector of the sphere, which would also be parallel to the longitudinal direction of a transducer installed at a given position. From (3.5), the radial displacement of the surface of the sphere is

$$z_j(t) = \hat{\mathbf{r}}_j \cdot \sum_m A_m(t)\Psi_m \tag{3.30}$$

The resonator R_{j1}, at position $\mathbf{r}_j$, will be displaced $z_j + q_{j1}$ and resonator 2 will displace $z_j + q_{j1} + q_{j2}$, as seen in fig 3.2. Since each transducer is located at a

Figure 3.2 - Body diagram of a system of a two mode resonant transducer coupled to the surface of a vibrating sphere.
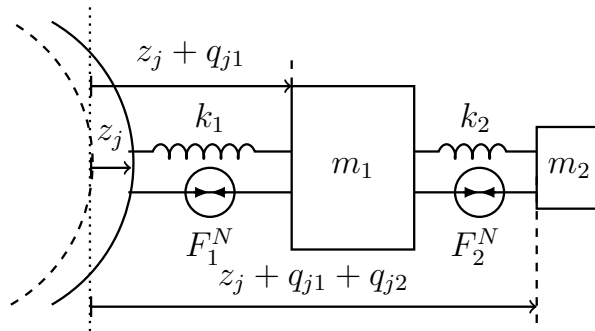
position (θ_j, ϕ_j), and each mode m contributes differently to the displacement of a point $u(\theta, \phi) \propto \sum_m Y_m(\theta, \phi)$ each transducer is excited by a different combination

of the modes. It is possible to denote the relation between the influence of the m-th mode and j-th transducer as a pattern matrix B_{mj} (JOHNSON; MERKOWITZ, 1993).

$$\alpha(R)B_{mj} = \hat{\mathbf{r}}_j \cdot \Psi_m(\hat{\mathbf{x}}_j) \tag{3.31}$$

Where α is the radial eigenfunction defined in (3.10a) evaluated at the surface $r = R$. Using the definition of Ψ (3.8), it simplifies to:

$$B_{mj} = Y_m(\theta_j, \psi_j) \tag{3.32}$$

For the TIGA arrangement[2], the following relations are true:

$$\underline{\underline{B}}\,\underline{\underline{B}}^T = \frac{3}{2\pi}\underline{\underline{I}} \tag{3.33a}$$

$$\underline{\underline{B}}\underline{1} = \underline{0} \tag{3.33b}$$

$$\underline{\underline{B}}^T\underline{\underline{B}} = \frac{3}{2\pi}\underline{\underline{I}} - \frac{1}{4\pi}\underline{\underline{1}} \tag{3.33c}$$

3.3.3 Equations of motion for sphere and resonators

The complete system of equations, that describe the motions of sphere and all resonators, derived using elasticity theory and notated using the pattern matrix is (COSTA, 2006)

$$\begin{pmatrix} m_S\underline{\underline{I}} & \underline{0} & \underline{0} \\ m_{R_1}\alpha\underline{\underline{B}}^T & m_{R_1}\underline{\underline{I}} & \underline{0} \\ m_{R_2}\alpha\underline{\underline{B}}^T & m_{R_2}\underline{\underline{I}} & m_{R_2}\underline{\underline{I}} \end{pmatrix} \cdot \begin{pmatrix} \ddot{\underline{A}}(t) \\ \ddot{\underline{q}}_1(t) \\ \ddot{\underline{q}}_2(t) \end{pmatrix} + \begin{pmatrix} H_S\underline{\underline{I}} & -H_{R_1}\alpha\underline{\underline{B}} & \underline{0} \\ \underline{0} & H_{R_1}\underline{\underline{I}} & -H_{R_2}\underline{\underline{I}} \\ \underline{0} & \underline{0} & H_{R_2}\underline{\underline{I}} \end{pmatrix} \cdot \begin{pmatrix} \dot{\underline{A}}(t) \\ \dot{\underline{q}}_1(t) \\ \dot{\underline{q}}_2(t) \end{pmatrix}$$

$$+ \begin{pmatrix} k_S\underline{\underline{I}} & -k_{R_1}\alpha\underline{\underline{B}} & \underline{0} \\ \underline{0} & k_{R_1}\underline{\underline{I}} & -k_{R_2}\underline{\underline{I}} \\ \underline{0} & \underline{0} & k_{R_2}\underline{\underline{I}} \end{pmatrix} \cdot \begin{pmatrix} \underline{A}(t) \\ \underline{q}_1(t) \\ \underline{q}_2(t) \end{pmatrix} = \begin{pmatrix} \underline{\underline{I}} & -\alpha\underline{\underline{B}} & \underline{0} \\ \underline{0} & \underline{\underline{I}} & -\underline{\underline{I}} \\ \underline{0} & \underline{0} & \underline{\underline{I}} \end{pmatrix} \cdot \begin{pmatrix} \underline{F}_S(t) \\ \underline{F}_1^N(t) \\ \underline{F}_2^N(t) \end{pmatrix}$$

$$\tag{3.34}$$

Where m_S is the mass of the sphere; m_{R1} is the mass of the 1st resonator; m_{R2} is the mass of the 2nd resonator; $\underline{A}$ is the vector of amplitudes of the modes of the sphere; $\underline{q}_1$ and $\underline{q}_2$ are the vectors of displacements of each type of resonators; H_X are the respective dampening coefficients and k_X are the elastic coefficients. α is the radial eigenfunction evaluated at the surface, $\underline{\underline{B}}$ is the pattern matrix B_{mj}. $\underline{F}_S$ are the forces acting on the sphere, $\underline{F}_i^N$ are the forces due to noises acting on the

---

[2]see Section 3.6

22

resonators. This system may be represented in the more compact fashion:

$$\underline{\underline{X}}\ddot{\omega}(t) + \underline{\underline{Y}}\dot{\omega}(t) + \underline{\underline{Z}}\omega(t) = \underline{\underline{W}}F(t) \tag{3.35}$$

3.4 Equations' solution

Starting with Equation (3.35) and multiplying all by $\underline{\underline{X}}^{-1}$, we arrive at:

$$\ddot{\omega}(t) + \underline{\underline{H}}\dot{\omega}(t) + \underline{\underline{K}}\omega(t) = \underline{\underline{P}}F(t) \tag{3.36}$$

It is possible to designate a matrix $\underline{\underline{D}}$ given by the diagonalization of $\underline{\underline{K}}$, where the pair $\underline{\underline{U}}$ and $\underline{\underline{U}}^{\dagger}$ are hermitian matrices ($\underline{\underline{U}}\,\underline{\underline{U}}^{\dagger} = \underline{\underline{U}}^{\dagger}\underline{\underline{U}} = \underline{\underline{I}}$).

$$\underline{\underline{D}} = \underline{\underline{U}}\,\underline{\underline{K}}\,\underline{\underline{U}}^{\dagger} \tag{3.37}$$

The elements of the diagonal matrix $\underline{\underline{D}}$ are the eigenvalues of $\underline{\underline{K}}$. Let's also define the normal coordinates $\underline{\xi}$:

$$\underline{\xi}(t) = \underline{\underline{U}}^{\dagger}\omega(t) \tag{3.38}$$
$$\omega(t) = \underline{\underline{U}}\underline{\xi}(t) \tag{3.39}$$

Now, if we multiply (3.36) by $\underline{\underline{U}}^{\dagger}$, it becomes

$$\underline{\underline{U}}^{\dagger}\ddot{\omega}(t) + \underline{\underline{U}}^{\dagger}\underline{\underline{H}}\dot{\omega}(t) + \underline{\underline{U}}^{\dagger}\underline{\underline{K}}\omega(t) = \underline{\underline{U}}^{\dagger}\underline{\underline{P}}F(t) \tag{3.40}$$

using definitions (3.37) and (3.38):

$$\ddot{\underline{\xi}}(t) + \underline{\underline{U}}^{\dagger}\underline{\underline{H}}\underline{\underline{U}}\dot{\underline{\xi}}(t) + \underline{\underline{D}}\underline{\xi}(t) = \underline{\underline{U}}^{\dagger}\underline{\underline{P}}F(t) \tag{3.41}$$

Applying a Fourier transform to take from time into frequency domain:

$$-\omega^2\tilde{\underline{\xi}}(\omega) + i\omega\underline{\underline{U}}^{\dagger}\underline{\underline{H}}\underline{\underline{U}}\tilde{\underline{\xi}}(\omega) + \underline{\underline{D}}\tilde{\underline{\xi}}(\omega) = \underline{\underline{U}}^{\dagger}\underline{\underline{P}}\tilde{F}(\omega) \tag{3.42}$$
$$\left(-\omega^2\underline{\underline{I}} + i\omega\underline{\underline{U}}^{\dagger}\underline{\underline{H}}\underline{\underline{U}} + \underline{\underline{D}}\right)\tilde{\underline{\xi}}(\omega) = \underline{\underline{U}}^{\dagger}\underline{\underline{P}}\tilde{F}(\omega) \tag{3.43}$$

And defining a matrix $\underline{\underline{J}}^{-1}$ to aggregate the terms

$$\underline{\underline{J}}^{-1}(\omega)\tilde{\underline{\xi}}(\omega) = \underline{\underline{U}}^{\dagger}\underline{\underline{P}}\tilde{F}(\omega) \tag{3.44}$$

Multiply by $\underline{\underline{J}}$ and $\underline{\underline{U}}$

$$\underline{\underline{U}}\,\tilde{\xi}(\omega) = \underline{\underline{U}}\,\underline{\underline{J}}(\omega)\underline{\underline{U}}^{\dagger}\underline{\underline{P}}\,\tilde{\underline{F}}(\omega) \tag{3.45}$$

and coming back from the normal coordinates

$$\tilde{\underline{\omega}}(\omega) = \underline{\underline{U}}\,\underline{\underline{J}}(\omega)\underline{\underline{U}}^{\dagger}\underline{\underline{P}}\,\tilde{\underline{F}}(\omega) \tag{3.46}$$

Here, the reverse Fourier can be used to obtain $\underline{w}(t)$, that will be the solutions to the equations of motion. They should be on the form

$$\underline{\omega}(t) = \underline{\underline{Q}}(\omega)\underline{F}(t) \tag{3.47}$$

$$\begin{pmatrix} \underline{\ddot{A}}(t) \\ \underline{\ddot{q}_1}(t) \\ \underline{\ddot{q}_2}(t) \end{pmatrix} = \underline{\underline{Q}}(\omega) \begin{pmatrix} \underline{F}_S(t) \\ \underline{F}_1{}^N(t) \\ \underline{F}_2{}^N(t) \end{pmatrix} \tag{3.48}$$

Where the components $\underline{q}_2$ – the ones that will be measured – are explicitly expressed.

3.4.1 Mode channels

The displacement of the second resonators q_2, despite being the quantity that will be measured, does not have a direct correlation with the incident gravitational waves. A much more direct comparison could be made if the measured quantity was related to the spherical modes. Thus, here are defined the mode channels:

$$g_m \equiv B_{mj}q_{j2} \tag{3.49}$$

or

$$\underline{g} = \underline{\underline{B}}\,\underline{q}$$

These are quantities that groups all resonators excited by a given mode.

3.5 Transfer function

To relate the displacement to the forces that cause them, we will need to describe the transfer function of the system. Using only the last components from (3.48):

$$\tilde{\underline{q}}_2(\omega) = \underline{\underline{\tilde{Q}}}_3(\omega) \begin{pmatrix} \tilde{\underline{F}}_S(\omega) \\ \tilde{\underline{F}}_1^{\,N}(\omega) \\ \tilde{\underline{F}}_2^{\,N}(\omega) \end{pmatrix} \tag{3.50}$$

or

$$\tilde{\underline{q}}_2(\omega) = \underline{\underline{\tilde{Q}}}_{3S}(\omega)\tilde{\underline{F}}_S(\omega) + \underline{\underline{\tilde{Q}}}_{31N}(\omega)\tilde{\underline{F}}_1^{\,N}(\omega) + \underline{\underline{\tilde{Q}}}_{32N}(\omega)\tilde{\underline{F}}_2^{\,N}(\omega) \tag{3.51}$$

and rewriting them in terms of mode channels (3.49)

$$\tilde{g}(\omega) = \underline{\underline{\tilde{\xi}}}(\omega)\tilde{\underline{F}}_S(\omega) + \underline{\underline{\Omega}}_1(\omega)\tilde{\underline{F}}_1^{\,N}(\omega) + \underline{\underline{\Omega}}_2(\omega)\tilde{\underline{F}}_2^{\,N}(\omega) \tag{3.52}$$

In this equation, $\tilde{g}(\omega)$ are the mode channels; $\tilde{\underline{\xi}}(\omega)$ is the transfer function of the detector in regard to the $\tilde{\underline{F}}_S(\omega)$ effective forces acting on the sphere. The relations of the responses to noises acting on the resonators and the forces are $\underline{\underline{\Omega}}_i(\omega)$ and $\tilde{\underline{F}}_i^{\,N}(\omega)$.

From Equation (3.52), if we ignore the contribution from noises now, we have:

$$\tilde{g}(\omega) = \underline{\underline{\xi}}(\omega)\tilde{\underline{\mathcal{F}}}(\omega) \tag{3.53}$$

As the forces can be written in terms of the modes (eq. 3.23)

$$\tilde{F}_m^{\text{eff}}(\omega) = -\frac{1}{2}\omega^2 m_S \chi R \tilde{h}_m(\omega) \tag{3.54}$$

Substituting (3.53):

$$\tilde{g}(\omega) = -\frac{1}{2}\omega^2 m_S \chi R \underline{\underline{\xi}}(\omega)\tilde{\underline{h}}(\omega) \tag{3.55}$$

Rewriting to find an expression of $\tilde{h}$ in terms of $\tilde{g}$:

$$\tilde{\underline{h}}(\omega) = -\frac{2}{\omega^2 m_S \chi R}\underline{\underline{\xi}}^{-1}(\omega)\tilde{g}(\omega) \tag{3.56}$$

The last step necessary to finally write $h_m(t)$ in relation to $g_m(t)$ is to apply the

inverse Fourier transform. Hence, it is possible to write an equation of form:

$$h_m(t) = \Xi_{mn}g_n(t) \tag{3.57}$$

In the same fashion, it would be possible to write a transfer function of a noisy detector as well, adding the contribution of the terms $\underline{\underline{\Omega}}_i$.

3.6 TIGA

After finding a way to measure the displacement of the surface of the detector, the next step is to determine where to install the transducers and how many there should be.

At first glance, one can be tricked by a "the more, the merrier" approach and try to fit as many transducers as possible on the surface to try to produce the highest resolution picture of the vibrations on the surface. But only a special set of the vibrations of the sphere are interesting for our purposes, that being the quadrupole modes of vibration.

A solid sphere has five purely radial quadrupole modes of vibration, and their functions form an orthogonal base so that a spheric detector can also be considered equivalent to five independent bar detectors. To monitor these, at least five transducers will be required. But since transducers are harmonic oscillator themselves, choosing a great number of them will imply in cross-coupling their equations of motions to the sphere and to each order. The analysis of the problem will become increasingly harder and the final spectrum turns out too complicated to be properly understood.

Depending on their position, a transducer might "see" the excitation of one or multiple modes. As they are pushed and pulled following the displacement of the surface, is evidence from Figure 3.1 that a region where a transducer is installed might be on the blind spot of a mode. Methods were developed to solve the inverse problem, that is, given the signal from multiple transducers that each are coupled to a combination of the quadrupole modes vibrations, find the direction and polarization of a gravitational wave that produced that excitation (LOBO, 1995; MERKOWITZ; JOHNSON, 1997). A single spherical detector can determine the direction, but cannot ascertain where the source is located between the two antipodal regions in the sky.

Turns out that six transducers in a Truncated Icosahedron (TI) arrangement produces a convenient basis given the number of symmetries, a not so complex frequency

26

Figure 3.3 - Truncated Icosahedron.
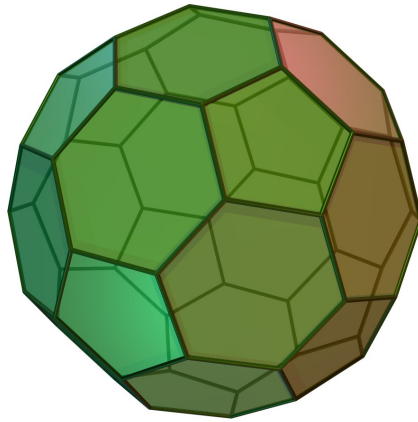
structure and is a shape not far from a sphere (MERKOWITZ; JOHNSON, 1995).

The truncated icosahedron is a solid made up of 12 regular pentagonal faces and 20 regular hexagonal faces (as represented in Figure fig:ti). The Truncated Icosahedron Gravitational wave Antenna (TIGA) is defined as a body with transducers plugged in holes located where the centers of the pentagonal faces of a circumscribed TI would be.

In the case of Schenberg, there are six transducers located following the map on Figure 3.4.

Figure 3.4 - Map of the positions of the holes on the surface of the antenna, using Lambert projection. Filled circles are the location where the 3.2khz parametric transducers are installed, following a TIGA arrangement. Unfilled circles are either empty or have transducers tuned to other modes, which are ignored in this work.
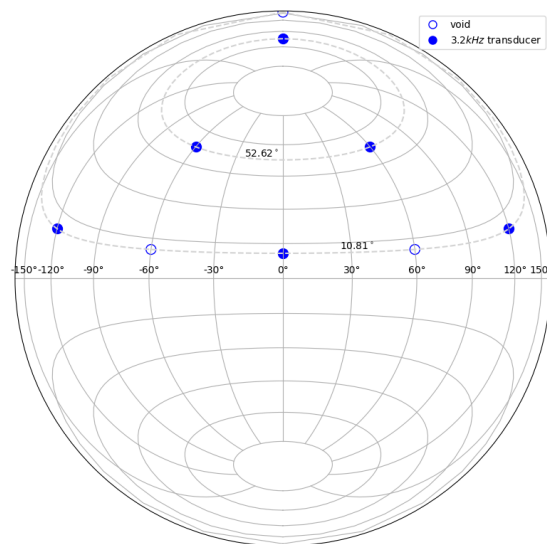
SOURCE: From the author.

4 THE MARIO SCHENBERG GW ANTENNA

4.1 Description of the antenna

The design of the antenna is a body of aluminium bronze (CuAl6%) based on a sphere of 325 mm with a central, cylindrical through hole along its vertical axis, which around its midpoint a small conical section serves as a load bearing face through were the body is suspended. Around its surface, 9 blind holes, located according to the description in Section 3.6. A render of the instrument can be seen in Figure 4.1

In those holes, 6 parametric transducers are installed. They are shaped roughly as a hollow cylindrical body. Its base has a diameter that enters snugly in the holes, so that the transducer is shrink-fit as the detector goes cryogenic. The mid-section has a turned down diameter and "speed holes" in order to make a spring that moves purely longitudinally. The membrane covers the top of the body and is clamped by the screws' action between the cap and the body. The features of the cap include a depression and conical post that forms a microwave cavity along with the membrane. Two holes in the cap allows for the pumping in and sensing of the

Figure 4.1 - Render of the assembled Schenberg detector.
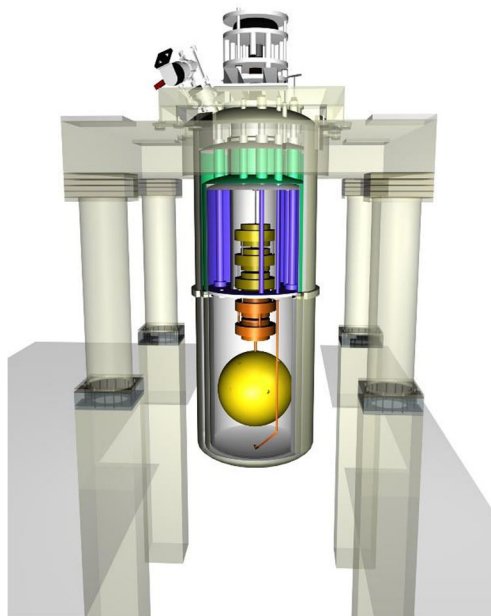
SOURCE: Aguiar et al. (2004)

microwave radiation. The transducer is composed entirely of pieces of niobium (body, membrane, cap and screws). The top part of the transducer is what is represented by the mass m_1 in the mathematical model (and Figure 3.2) and the membrane is m_2. The intended operating temperature is 15 mK, achievable with the help of a dilution refrigerator. The antenna is installed suspended by a vibration isolation system, inside a vacuum chamber, which is also has its own isolation from the ground.

4.2 Previous models

It's a well established result that the spherical harmonics of order $l = 2$ (quadrupoles) are comprised of five orthonormal functions, being two pairs and a singlet, all degenerate (same energy, same frequency) (JACKSON, 1999). For a real elastic body with a geometry that deviates from the ideal sphere the structure of these frequencies is not guaranteed to be as simple.

Finding the natural modes of vibration for bodies of complex geometry is an arduous task, if someone wants to find an analytical solution directly from the theory of elasticity of continuous bodies (LANDAU, 1981). Luckily, there are numerical methods that can produce these results, as is the case of the Finite Element Method (FEM). This approach consists of approximating a continuous body by a collection of elements distributed along a mesh and modeling how these elements will interact with its neighbors.

Previous works used FEM with models constructed from the engineering drawings of the antenna and definitions of materials properties are found in the literature (BORTOLI, 2011; BORTOLI et al., 2021). Degeneracy breaking was predicted when geometrical features of the antenna were introduced to the spherical body (Figure 4.2). Also, a preferential direction was observed in the orientation of the basis of the modes, since the body lost spherical symmetry while keeping cylindrical symmetry.

The values for the quadrupole modes of the 3 described simulated cases are listed in Table 4.2. A small allowance has to be considered for the errors that arise from the discretization of the continuous body. The results can differ slightly for the same model if the meshing parameters are changed.

In column a), for instance, all the frequencies are virtually the same, which is expected for an ideal sphere. In column b), the same applies. Possibly, the mass lost when drilling the holes was not enough to make a visible difference.

The frequencies in column c) are grouped into two degenerate pairs and an isolated

Table 4.1 - Results from Bortoli (2011). Values from Schenberg's FEM simulations to find the frequencies of natural modes of vibration. The modes corresponding to quadrupoles were identified and the values for their frequencies were transcribed here. Columns a), b) and c) corresponds to different geometric features of the model (see fig. 4.2). The last column shows the measured quadrupole frequencies from the first commissioning run (AGUIAR et al., 2004).

a) Solid sphere (simulated)	b) Sphere with holes for transducers (simulated)	c) Sphere with holes for transducers and suspension (simulated)	Suspended antenna w/o transducers (experimental)
3157.87	3159.38	3117.93	3172.50
3157.95	3159.49	3118.23	3183.00
3158.06	3159.55	3138.27	3213.60
3158.21	3159.65	3138.45	3222.90
3158.32	3159.84	3155.59	3240.00

SOURCE: Bortoli (2011), Aguiar et al. (2004)

mode. If we compare the exaggerated representation of the spherical harmonics from Figure 3.1 and the mass distributions of the body model c) in Figure 4.2 we'll start to make some sense of why this grouping happens, at least from a qualitative standpoint.

4.2.1   A qualitative example

To help keep in mind that these bodies are not perfectly modeled by the spherical harmonic functions anymore and to choose a set of characters that allow a more direct pictorial representation of the underlying physics, from now on I'll be using the following notation to symbolize the quadrupole modes of quasi-spheric bodies[1]. Since there is rotational symmetry around the vertical axis, I'll designate it a north-south axis and use words such as "equator", "northern" and "southern hemispheres" and other geographical terms when suitable. For $m = \pm 2$: $\oplus$ and $\oplus'$; for $m = \pm 1$: $\otimes$ and $\otimes'$; finally, for $m = 0$: $\odot$. The primed symbol denotes a rotation around the vertical ($\pi/2$, a priori). To represent a mode that could not be identified I'll use $\bigcirc^?$.

Assuming the holes on the surface are perfectly located and drilled, there should be no practical distinction on the mass distribution to define a plane that bisects the body (c) of Figure 4.2 into "oriental" and "occidental" hemispheres. Therefore, the

---

[1]I'll use this terminology when describing any body that is derived from a solid sphere within a limited number of operations, while still mantaining overall roundness

Figure 4.2 - Isometric rendering of the section of three quasi-spheric bodies with different features studied in a previous work.

a)　　　　　　b)　　　　　　c)
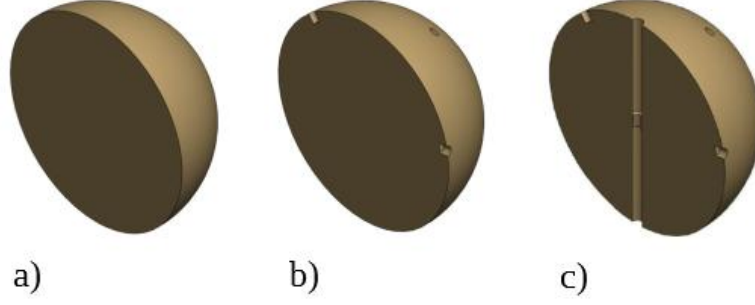
non-prime and prime modes are still degenerate.

Each mode frequency is more sensitive to the participation of a mass element where their displacement is greater. For modes $\oplus$ and $\oplus'$, corresponding to the modes $Y_{2\pm2}$, the solutions for radial displacement in respect to the spherical coordinates angles are

$$Y_2^{-2}(\theta, \phi) = \frac{1}{4}\sqrt{\frac{15}{2\pi}} \cdot e^{-2i\phi} \cdot \sin^2\theta \tag{4.1}$$

$$Y_2^2(\theta, \phi) = \frac{1}{4}\sqrt{\frac{15}{2\pi}} \cdot e^{2i\phi} \cdot \sin^2\theta \tag{4.2}$$

Averaging the variation along ϕ, these modes will have no displacement when $\theta = 0$ and maximum for $\theta = \pi/2$. Both functions are also symmetric in respect to $\theta = \pi/2$ in the range $(0, \pi)$, because of $\sin^2\theta$.

For modes $\otimes$ and $\otimes'$, corresponding to the modes $Y_{2\pm1}$, the solutions for radial displacement in respect to the spherical coordinates angles are

$$Y_2^{-1}(\theta, \phi) = \frac{1}{2}\sqrt{\frac{15}{2\pi}} \cdot e^{-i\phi} \cdot \sin\theta \cdot \cos\theta \tag{4.3}$$

$$Y_2^1(\theta, \phi) = -\frac{1}{2}\sqrt{\frac{15}{2\pi}} \cdot e^{i\phi} \cdot \sin\theta \cdot \cos\theta \tag{4.4}$$

Averaging the variation along ϕ, these modes will have no displacement when $\theta = \pi/2$ and maximum for its absolute value for $\theta = \pi/4, 3\pi/4$.

For modes $\odot$ corresponding to the mode Y_{20}, the solutions for radial displacement in respect to the spherical coordinates angles is

$$Y_2^0(\theta, \phi) = \frac{1}{4}\sqrt{\frac{5}{2\pi}} \cdot \left(3\cos^2\theta - 1\right) \tag{4.5}$$

Other than no dependence of phi, this mode has maximum displacement when $\theta = 0$ and maximum for its absolute value for $\theta = \pi/4, 3\pi/4$.

Not only that, but their derivatives in respect to θ around 0 will would indicate that even as modes m = 1 and 2 have a node around 0, for any value $\gtrsim 0$ the behavior is already different enough to warrant a degeneracy break.

If these intuitions are correct, a small conical cut from the surface to the center (independent of Γ $and \phi$) of a once perfect solid sphere would break degeneracy between 2, 1 and 0. That would also be the case if an inverted conical trunk was added somewhere on the surface. In both cases, a preferential axis of symmetry would appear, aligning the $\theta = 0$ axis from the harmonics to the revolution axis.

As a conjecture, any small deformation, adding or removing mass in such a way that spherical symmetry is lost, but cylindrical symmetry is maintained would produce a similar effect on the frequency structure.

Running a quick simulation indicates that this is the case. From a model of the solid CuAl sphere from Figure 4.2 (a) a model was generated. The simulated material now is slightly different, but still is the accepted range of values for this alloy, hence why the values differ from Table 4.2. Only the arrangement of the frequencies is of interest in this section. The render of this model and of some of its modes is shown

in Figure 4.3. The results for the values of the frequencies for the five quadrupole modes are in Table 4.2.

Figure 4.3 - Representation of the quadrupole modes in a FEM simulated quasi-sphere with a conical plug removed.
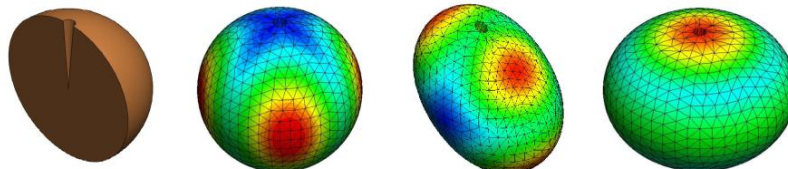
SOURCE: From the author.

Table 4.2 - Frequencies of quadrupole modes of a CuAl6% quasi-sphere with azimuthal symmetry. As stated previously, a small allowance must be made for the discretization errors and should consider $f_\oplus = f_{\oplus'}$ and $f_\otimes = f_{\otimes'}$.

Mode	Frequency (Hz)
$\oplus$	3268.1
$\oplus'$	3268.8
$\otimes$	3277.6
$\otimes'$	3277.6
$\odot$	3285.1

SOURCE: From the author

With this in mind, it should be no surprise that the addition of the vertical through hole would at least break the frequency structure into the $2 + 2 + 1$ grouping as the simulations by Bortoli (2011) had already shown.

No assertion can be made here on the ordering of these groups.

4.3 Challenges for the Schenberg project

The sensitivity curves calculated so far for the detector consider an analytic model that assumes the antenna as a solid sphere. These calculations consider the coupling

34

of the five degenerate modes to single-mode resonant transducer of the same frequency (MERKOWITZ; JOHNSON, 1995) or to two-mode resonant transducer (COSTA, 2006).

In the latter case, these couplings produce a structure of frequencies comprised of 17 resonant frequencies centered around the sphere quadrupole frequency. Much work was also done to study the effect of noise sources and how they are added to the signal (ANDRADE, 2001; ANDRADE et al., 2004; FRAJUCA et al., 2004) and what would this mean for the determination of the properties of the gravitational radiation (MERKOWITZ; JOHNSON, 1997).

However, there is a problem that arises when trying to match the frequency arrangements from the models cited above with what was measured so far. The analytical model for the isolated antenna, that assumes degenerate quadrupole modes, assumes the resonant frequency at $3206.3\,\text{Hz}$ (COSTA, 2006)). The FEM model from Bortoli (2011) predicts modes at $(3117.93, 3118.23, 3138.27, 3138.45, 3155.59)\text{Hz}$, which averages at $3133.69\,\text{Hz}$ and has the $2 + 2 + 1$ characteristic structure. The data from Aguiar et al. (2008), however, indicates that the resonant frequencies of the quadrupoles of the antenna are $(3172.50, 3183.00, 3213.60, 3222.90, 3240.00)\text{Hz}$ with $\langle f \rangle = 3206.4\,\text{Hz}$. And not only all values are different, be no pattern can be seen in the distribution of the frequencies.

Furthermore, work by Gottardi et al. (2007) on the results obtained by MiniGRAIL identified the resonant modes of the antenna coupled to the transducers, but without explanation on how they were structured. Although the number of detected modes was right, given the number of transducers installed in that situation, the explanation for how they were distributed position was not conclusive. The paper indicated that the root cause was the cross-coupling between the transducers, whose tuning differed ever so slightly, but did not propose a model capable of reproducing those results. Despite being a sound argument from a physics perspective, there is reason to believe that perhaps there is at least another effect at play here.

On the next chapter, this problem will be addressed with models that could explain, at least partially, this behavior.

5 A NEW MODEL

As the data indicates, the five modes of the antenna seem to be non-degenerate (AGUIAR et al., 2008). As shown in Section 4.2, allowing the mass distribution for breaking the spherical symmetry did affect the distribution of the frequencies. Perhaps, it is a good idea to keep the concept of breaking symmetries.

As was done before with θ, it is worth considering what's the role of ϕ in the spherical harmonics equations.

The easiest bit to consider is that

$$\frac{\mathrm{d}Y_2^0}{\mathrm{d}\phi} = 0 \tag{5.1}$$

For the modes $m = \pm 1$, the dependence in ϕ in these two modes differs since:

$$Y_2^{-1}(\theta, \phi) \propto e^{-i\phi} \tag{5.2}$$

$$Y_2^1(\theta, \phi) \propto e^{i\phi} \tag{5.3}$$

And since the sphere eigenfunctions are dependent on the harmonics, and we're trying to understand how a different mass distribution will affect differently the modes of oscillation, it serves at least as an indication that, a break of symmetry in ϕ could result, given the equations of motion, in breaking their pair degeneracy.

There is no indication of how the modes from the empirical results are ordered. But, from now on, I'll assume that the two lower and two middle frequencies are the two duplets (equatorial $\oplus$ and oblique $\otimes$, for simplicity) and the highest is the singlet (prolate-oblate $\odot$).

In the rest of this chapter, two main hypotheses will be considered. To produce a mass distribution that lost azimuthal symmetry, perhaps either the geometry is still symmetric, but the material is inhomogeneous or the geometry itself. is not symmetric , therefore, from the start may not be able to consider homogeneity

5.1 Influence of variations of the material properties

One of the main assumptions made when modeling the antenna is that the physical properties of the material are homogeneous and isotropic. However, this is just a simplification that allows us to develop the theory of elastic bodies in a much simpler

way. So, when the models are not capable of reproducing the results obtained from experiment perhaps it's time to challenge this assumption.

The body of the antenna was made from a bronze monolith that was cast and then machined. Both of these processes have precedents of suffering from effects that produces non-homogeneous materials. As the material is poured into the crucible, the molten metal cools differentially in different points of the pour. The regions that are closer to the walls and bottom of the crucible will exchange heat differently from the top, that is exposed to air. As solubility is a property dependent on the temperature, the kernels of the crystalline structure have a slightly altered composition from the exterior frontiers of the grain (while also depending on the position in the body). Furthermore, gravity also plays a role in the way the composition vary vertically. The freezing of the liquid also introduces strains between the regions – and that would change in posterior heat treatments (CAMPBELL, 2015).

Although the formation of bubbles and cracks are also well known defect of the casting process, there is no evidence to consider that this is the culprit. The high mechanical factor that was measured, in addition to no sight of porosity in the machined surfaces led us to believe that a good stock was obtained from the pour.

The machining could also cause the work hardening of the regions near the surface of the body, specially considering that it is composed of an alloy of copper, a metal well known for suffering from this problem (CALLISTER; RETHWISCH, 2014).

Following this rationale, there are two ways to proceed. The first would be to try and sample pieces from several spots of the original stock for their physical properties through metallurgical analysis. There are several challenges here. First, there is the feasibility of conducting this research given the timetable of this work and the assets in our laboratory. And then there are the limitations of conducting non-destructive measurements of the antenna or being restrained by the samples that could be sacrificed.

The other route would be to try to model the effects of a heterogeneous body in the final antenna. Even if little information could be retrieved from this model on the exact nature of the distribution of the mechanical parameters around the body, a toy model of sorts could at least suggest if this would be a feasible explanation for the problem of the frequencies' distribution. And that was chosen and will be presented in the next section.

5.1.1 Heterogeneous model simulation

A realistic model of how the properties could vary given the manufacturing history of the detector would be a difficult challenge to overcome. The first step would involve modeling a cylindrical stock of cast aluminium bronze and how the chemical and physical properties would evolve during cooling and crystallization. This stock would then be reduced to a quasi-spherical body, in a way that could introduce work hardening. Given that there is no reason to pursue this level of detail before either a qualitative evaluation or exhausting other possible explanations, the model simulated here is simple, albeit unrealistic.

Instead of considering a model containing a gradient of a given property, these simulations introduces different regions with a discontinuous interface, each homogeneous in themselves. To do this, I'll start with the model that was drawn previously in SolidWorks by Bortoli (2011). The body of the antenna was sliced into eight octants, following the cartesian XYZ planes at the origin, as shown in Figure 5.1.

Figure 5.1 - Drawing of the sliced antenna body.
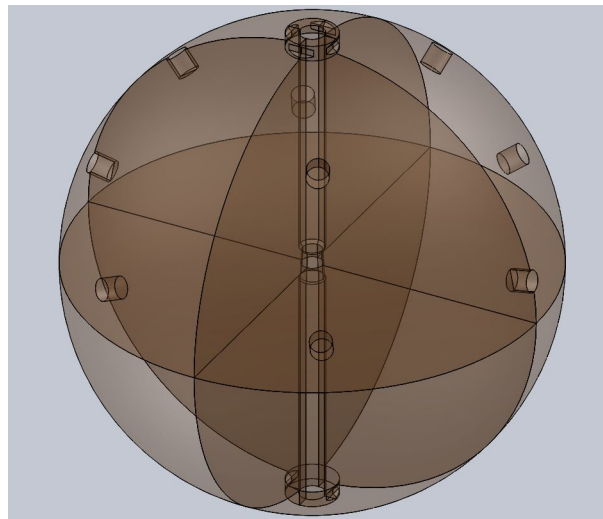
SOURCE: From the author.

For the simulation, the body was composed of combinations of slices that were attributed different materials. All were derived from a base material of Poisson's ratio 0.3 and density of $8077.5 \, \text{kg/m}^3$, the only changing parameter was the Young's module.

The objective was to obtain mode frequencies as close as possible to the 2004's results. So, in each step a change was introduced to the Young's module of one or more octants that I believed would lead closer to the goal.

Eventually, all quadrupole modes' frequencies obtained were within 1% of the desired frequency, as shown in 5.1. As this exercise was more qualitative in nature, no further effort was spent in fine-tuning nor in exploring changes in other material properties or chopping the body in more parts.

The lesson that can be extracted here is that the explanation for the frequency arrangement of the quadrupoles of the quasi-sphere could be, at least in part, due to a heterogeneous material. The confirmation of this hypothesis would require the metallurgical analysis of some samples of the stock and computational power to produce a higher resolution FEM model capable of including a more realistic elastic body.

If confirmed, perhaps a revised sensitivity curve would be required. It should allow for corrections in $\rho(\mathbf{r})$, $\lambda(r)$ and $\mu(r)$. From the equations of motion that where shown in Chapter 3, this will influence the elements of matrices $\underline{M}$, $\underline{K}$ and $\underline{C}$, that are themselves linked to the transfer function of the equipment.

5.1.2 Density of the sphere

Another issue encountered as these models were constructed was the fact that the value of density of CuAl6% is inconsistent between publications and was never properly verified. Some examples of the values used range from $7073 \, \text{kg/m}^3$ to $8077 \, \text{kg/m}^3$ (ANDRADE, 2001; BORTOLI, 2011).

It would be cumbersome to do any weight measurements on the > 1ton body. Luckily many other parts were produced from stock from the same pour. If we assume that the composition is about the same across all castings, it would be possible to produce a good estimation of the density of the antenna.

Here, a frame on top of a scale suspended a piece of aluminium bronze through a steel wire of negligible volume. As a vessel with water was introduced to envelope the body and water was displaced, a difference was registered on the scale. Figure 5.2 shows a picture of the process. Using Archimedes' principle and averaging out measurement from multiple pieces, the calculated value for density is $\rho = (7.96 \pm .02)\text{g/cm}^3$.

Table 5.1 - Frequency of quadrupole modes in a heterogeneous quasi-sphere. Results of FEM simulations of the antenna body divided into octants of different materials. In each row, a different body was simulated. The letters indicate which combinations of materials were chosen for the octants. The position of the letter indicates the position of the octant, starting of top-left-front octant and spiraling downward. The Poisson's ratio is 0.3 and density of $8077.5\,\mathrm{kg/m^3}$, the Young's moduli are named as $\underline{n}$eutral $= 1.345\times10^{11}$ Pa; $\underline{s}$tronger $= 1.4\times10^{11}$ Pa; $\underline{w}$eaker $= 1.3\times10^{11}$ Pa; $\underline{W}$eakest $= 1.25\times10^{11}$ Pa. The color of the cell indicates proportional difference from the 2004 empirical results. Green means closer, red means worse. The undivided model is the benchmark "classical" FEM model.

2004 results	3172.49	3183.00	3213.62	3222.90	3240.00
undivided model	3225.4	3226.4	3254.6	3255.1	3269.6
nnnnnnnn	3230.2	3231	3255.2	3255.6	3267.9
snnnnnnw	3232.1	3232.5	3256.8	3258.1	3269.9
swnnnnnn	3231.6	3232	3254.6	3259.3	3269.8
sswnnnnn	3239.0	3240.1	3264.8	3266.8	3278.6
wwwwsnnn	3214.1	3215.3	3235.3	3238.4	3248.3
wwwwsnnw	3205.9	3207	3229.5	3231.3	3242.2
Wwwwsnnw	3198.9	3199.7	3221.6	3223.3	3233.5
WWwwsnnw	3192.7	3193.6	3214.5	3215.5	3225.5
WWwwwwns	3184.9	3186.3	3207	3212.2	3221.6

SOURCE: From the author.

5.2 Influence of variations of the geometry

Other than changing the properties of the material, a mass distribution will change if the position of the mass elements change, i.e. if the body has a different geometry.

This section challenges the assumption that the body of the antenna is derived from an ideal sphere on which surface features were added. As discussed in 4.2.1, adding holes or bumps in the surface is enough to break degeneracy. Now, the goal is to use these features to fine tune the quadrupoles frequencies to match a desired set.

To try and reproduce the results from 2004, an arbitrary mass distribution was constructed that behaved the same – in terms of frequency arrangement of quadrupole modes – to the empirical results.

5.2.1 Arbitrary round shape

In this first attempt I won't bother with the practicality aspect of the model. The goal here, other than obtained the desired frequencies, is to develop the sensibility

Figure 5.2 - Picture and diagram of the process for determining density. A sample of the
CuAl alloy was suspended from a wire of negligible mass and volume, con-
nected to a frame that sits atop a scale. As a bucket of water is inserted
beneath then submerges the sample, the scale should register the weight of
displaced liquid.
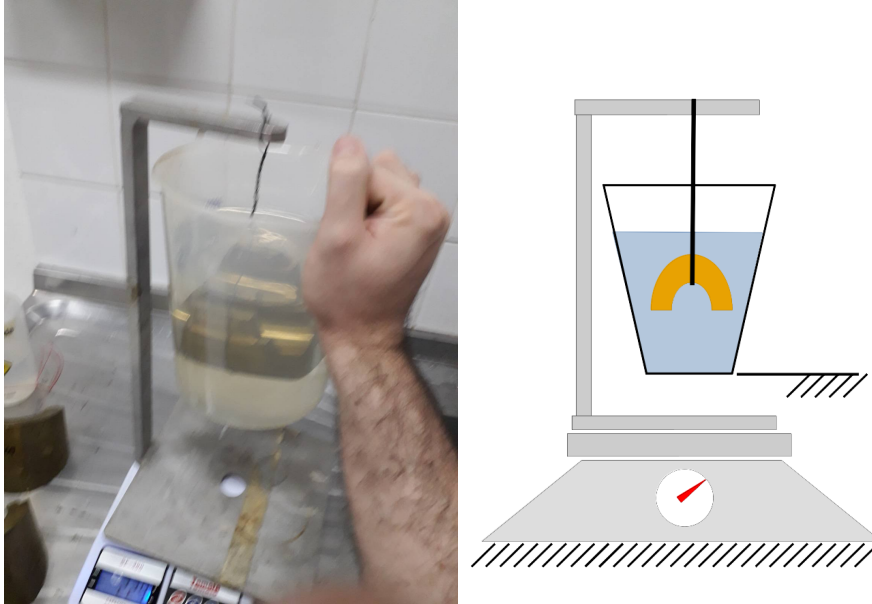
SOURCE: From the author.

of how different geometries impart different responses in frequency.

The rule of thumb to follow in order to tune the quasi-sphere is that, as each
quadrupole has regions where deformation is maximum and minimum, changing
the amount of mass in these regions will have much or no impact, respectively. As
in, a mode can be "sensitive" to the presence of mass in a region and "blind" to
another. And as would be expected from all spring-mass models, adding mass will
lower that frequency, removing mass will raise it.

An extra consideration has to be made in regions that will affect the behavior of
multiple modes.

At the time, as I was exploring alternative mechanical coefficients as a way to change
the arrangement of frequencies, these simulations was done using a material slightly
different from the one used by Bortoli (2011), hence the difference from the results
of similar geometry presented on Table 4.2. Since the objective of this work is to

explore the behavior of the frequencies in a macro scale, it is safe to proceed and the results can be compared taking this into account. With this in mind, let's start with a solid sphere of CuAl6%, 65cm in diameter. Then, the central hole and flanges were added. Followed by bands of a straight profile and cylinders normal to the surface. These steps are shown in Figure 5.3 and the results in 5.4.

Figure 5.3 - Process of adjusting frequencies for quasi-sphere. a) Started with sphere, b) added central hole, c) added flanges to central hole, d) band on the equator, e) disc on the equator, f) disc on the opposite side and lower hemisphere, g) band on the upper hemisphere. Primed indexes are the respective views with section. * is rotated around the vertical axis to show detail. The results are presented in Table 5.2.
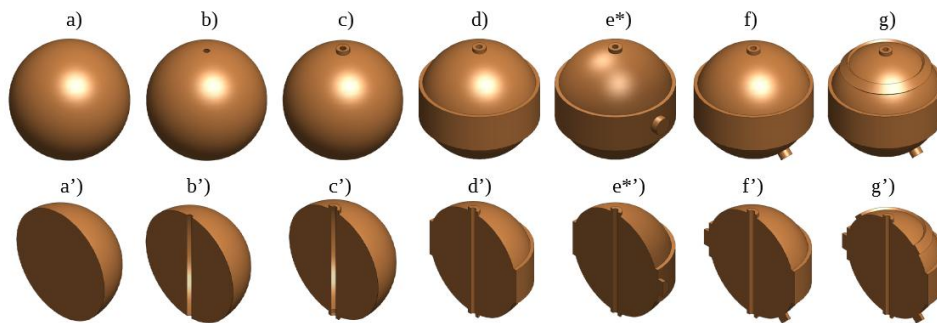
SOURCE: From the author.

It was not difficult to develop an art that allowed to quickly reach the desired stage. The simulated mode frequencies for each step are presented in Table 5.2. The solid presented in step g has the frequency arrangement that approximates the most the experimental results.

5.2.2 Alternative round shapes

To indicate that the geometry obtained in the previous section was not special, that its, to show that there are multiple quasi-spherical geometries that could have the same quadrupole modes frequency distribution, two additional models were proposed.

As the same as before, both went through an iterative process where changes that

Table 5.2 - Frequencies of quadrupole modes in the process of adjusting frequencies for quasi-sphere. Reference Figure 5.3. Each step I tried to get closer to the 5 modes of 2004 The color of the cell indicates deviation from 2004 empirical results. Green means closer, red means worse. Undivided model is the benchmark "classical" model from previous works, although considering another alloy.

a)	3276.6	3277	3277.1	3277.5	3277.7
b)	3243.7	3244.6	3261.6	3261.9	3275
c)	3175.8	3176.2	3220.1	3220.8	3241.7
d)	3177.5	3177.8	3220.4	3220.9	3241.4
e)	3176.4	3176.8	3220.9	3221.2	3242.3
f)	3171.2	3176.2	3220	3221.3	3240.6
g)	3170.2	3175.8	3218.5	3221.2	3240.1
Results 2004	3172.49	3183	3213.62	3222.9	3240

SOURCE: From the author.

brought it closer to the desired specifications were incrementally added.

The two models are called "sea mine" – arrays of cylinders glued to the surface as the spikes of a sea mine – and "ribs" – protrusions of semicircular profile that go around circles parallel to the plane of the equator. Both are represented in Figure 5.5.

It is worth mentioning that the choice of meshing has an effect on the simulated frequency values, as is seen in Figure 5.6. In conclusion, it is possible to chose multiple geometries that deviates from the original design of the antenna and that has the same (or almost) quadrupole modes frequencies as measured empirically. Therefore, it is reasonable to consider that perhaps the shape of the physical antenna is not exactly as designed and this would explain (at least partially) the frequency arrangement that is observed.

5.2.3 Ellipsoidal shapes

The models presented in the previous section were useful for giving an insight of what could be the root cause of the difference between the frequency arrangement of simulated original model and the measured results. But those models weren't a realistic representation of what could have happened with the antenna.

To search for possible culprits, one must understand how the antenna was machined. The initial bronze cylinder was turned down in a vertical lathe to a hemisphere. Here, the usual limitations on the tolerances achievable by the machine apply, so the final

Figure 5.4 - Frequencies distribution of the models presented in Figure 5.3 and comparison with the adapted FEM model (BORTOLI, 2011) and experimental results (AGUIAR et al., 2004).
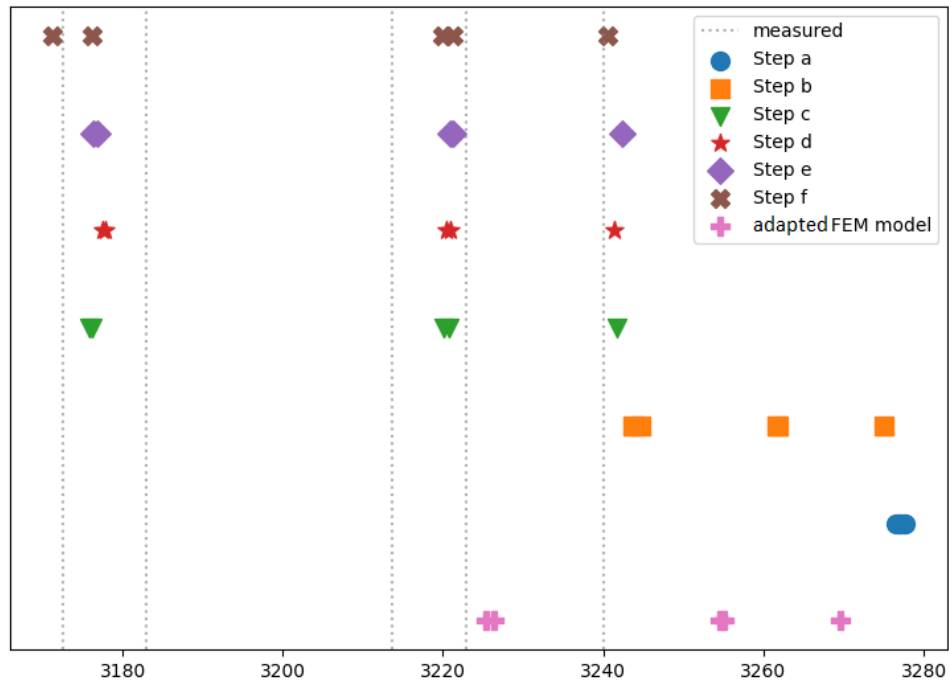
result will only be as spherical as the setup allows. Later, the piece is flipped, so the hemisphere is being held and the rest of the cylinder is machined down. Flipping a piece in such manner can introduce offset and misalignment errors between the actual and former revolution axis. These will be minimized by the machinist, but never eliminated.

To create a model that might simulate these and other manufacturing limitations, I'll assume that the body of the antenna can be approximated by an ellipsoid. To include the possibility of breaking the most symmetries, some cases will consider that all axes have different lengths ($a \neq b \neq c$).

The CAD model was reconstructed using two arcs of ellipses, drawn concentrically in two perpendicular planes in such way that the plane defined by the axis of the ellipsis is orthogonal to the first two. In the third plane, another arc of ellipsis, concentric

45

Figure 5.5 - "Sea mine" and "ribs" models.
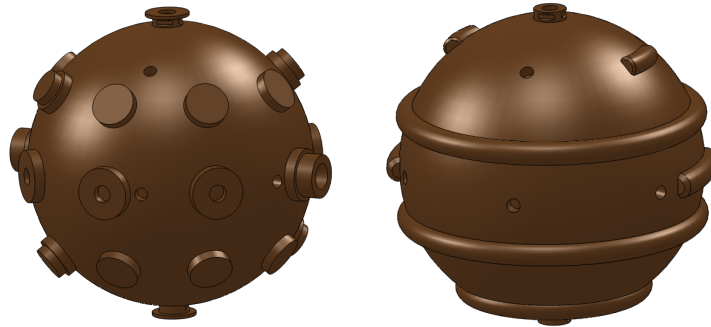
SOURCE: From the author.

and connecting the first two arcs. Using an interpolation function ("loft") of the software, a quarter of the ellipsoid was build. With some mirror operations and steps to recreate the remaining features of the body, and this model of the antenna was finally achieved. Furthermore, the system of coordinates comprised of planes of the ellipses could be misaligned in relation to the $\hat{\mathbf{z}}$ axis. Figure 5.7 shows a sketch of the model. To change the shape of the ellipsoid, it is only needed to change the length of the ellipses axes and everything else is automatically recalculated.

Again, the technique was to evolve the model to get closer to the results from the 2004 experiment. The results of the FEM simulation are presented in Table 5.2.3.

Once more, it was not difficult to change the geometries through trial and error until one satisfies the frequency distribution. And, in the end, despite the fact that the final shape is unrealistic, and such exaggerated deformation would already be known, this result makes necessary to quantify how much the physical antenna deviates from the spherical model.

5.2.3.1 Measurements of sphericity of the antenna

A spherometer, a piece of equipment devised to measure a radius of curvature, was built to verify how aspheric is the body of the antenna (Figure 5.8). If the manufacturing produced a piece perfectly true to the original design, the spherometer should register a radius of 325.00mm at any point, supposing the surface features are avoided.

The construction of the spherometer is straightforward. A square "C" frame touches

Figure 5.6 - Frequencies distribution of the "sea mine" and "ribs" models as simulated by
FEM. 3 runs for each, accounting different meshing parameters.
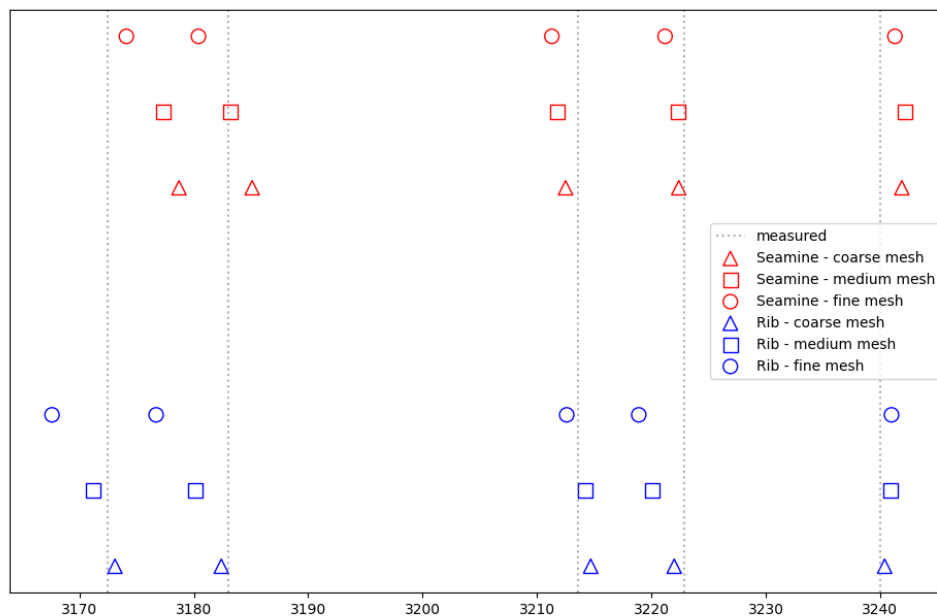
the surface of the sphere in two points, and a depth micrometer located at the arch's midpoint is able to measure the sagitta of the curve, as represented in Figure 5.9. Once that is known, it is possible to use some simple geometric relations to determine the radius of that arc. From Pythagoras theorem, the following equation is derived:

$$R = \frac{1}{2} \left(\frac{(d/2)^2}{g+z-h} + g+z-h \right) \tag{5.4}$$

With the spherometer in hands, the radius of curvature was measured around the antenna. Due to the existence of the holes and flanges, not all regions of the sphere were suitable. Also, the body is supported on a pedestal that restricts the access to the southern hemisphere.

Since the objective of this measurement is to first establish the average sphericity of the antenna and not to construct an exact map of its topology, the location of the

Figure 5.7 - Ellipsoid model of the antenna.
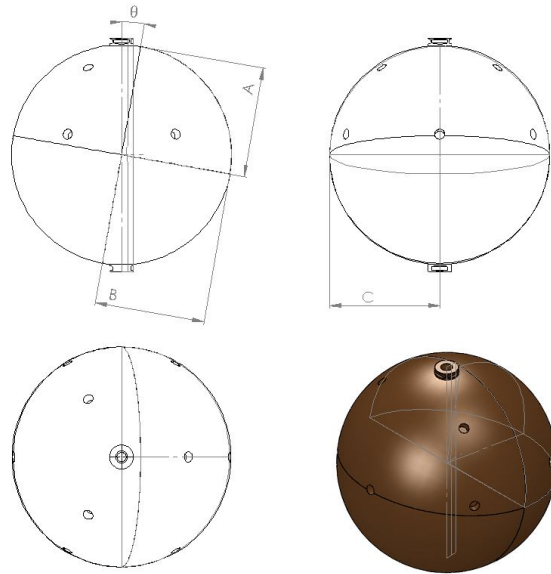
SOURCE: From the author.

points is not exact. It was enough to distribute them as evenly as possible around the surface. They are located around three circles parallel to the equator (Top: $\sim +10°$, near the holes on near the equator, Mid: $\sim +52°$, near the northern holes, and Bottom: $\sim -45°$ as far as the pedestal would allow). In each circle, 6 points, following the meridians defined by the holes on the surface (around 60° between each other).

Another test for sphericity is that the value for curvature at a point should not vary with the orientation of the instrument. Hence, for each point, the radius was measured twice, rotating the spherometer circa 90° around the normal of the sphere. In tables 5.2.3.1 and 5.2.3.1 the arrow symbols show the alignment of the spherometer and the local cardinal directions on the surface ($\updownarrow$: north-south and so on). The choice of the directions was limited by the presence of the surface features and the pedestal.

Much care was taken during measurement to guarantee that the instrument was as normal as possible from the surface, without introducing any bend or twist. To hold the instrument against the piece, without causing a sag, the arch was held with multiple pieces of adhesive tape, always kept taut and consistent between measure-

Table 5.3 - Parametric model of ellipsoid shaped antenna. *A*, *B* and *C* are the length of the semiaxes, in mm. θ is the angle of between the axis of length *A* and the vertical.

	A (mm)	B (mm)	C (mm)	θ (deg)	Modes $\oplus$	$\oplus'$	$\otimes$	$\otimes'$	$\odot$
2004 data	-	-	-	-	3172.5	3183.0	3213.6	3222.9	3240.0
Ellipsoidal models	325	325	325	0	3225.4	3226.4	3254.6	3255.1	3269.6
	330	325	325	0	3220.7	3221.3	3232.5	3233.3	3241.8
	330	330	325	0	3197.3	3198.7	3211.3	3227.7	3233.8
	330	330	325	5	3197.0	3199.3	3211.8	3228.3	3233.6
	330	325	325	5	3220.4	3220.9	3232.4	3234.2	3241.8
	330	325	320	5	3236.0	3236.4	3243.3	3256.6	3259.1
	330	330	325	10	3196.1	3198.5	3212.1	3228.3	3234.5
	330	325	325	10	3219.4	3219.6	3233.5	3233.7	3243.0
	330	325	335	10	3172.5	3179.4	3190.5	3222.0	3226.8
	330	325	332	10	3187.6	3191.7	3202.9	3224.9	3229.8

SOURCE: From the author.

ments.

Another issue was due to the geometry of the corner of the foot of the spherometer. Since it was a straight edge that made contact only on one point against a curved surface, some effort was spent to balance the instrument.

Also, as the thimble was rotated and the probe made contact with the surface, the normal force was enough to lift one of the foots of the frame. So, the micrometer was adjusted, so the ratchet would disengage with the smallest amount of force possible, and the frame was pushed gently to be kept in place.

Using the data presented in Table 5.2.3.1 and the Equation (5.4), the radius of curvature for each position and direction was calculated. These results are shown in Table 5.2.3.1.

This experiment showed two new pieces of information. First, the antenna is much more spheric than the cases being considered in the simulations made last section, with a radius of curvature $R = 323.3^{+.2}_{-.3}$ mm. And secondly, the value being considered for the radius in all previous work (325 mm) is wrong.

Figure 5.8 - Photo of the spherometer.
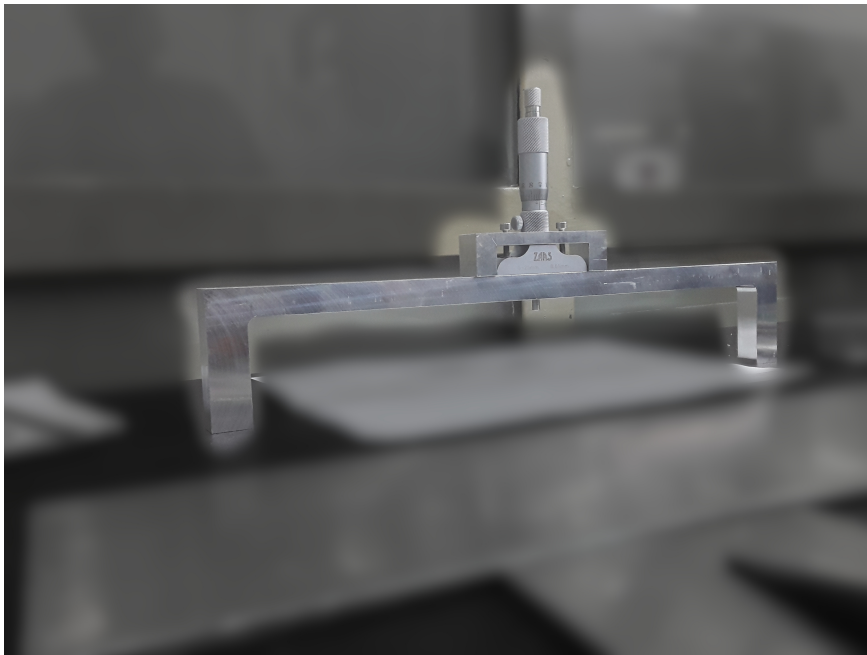
SOURCE: From the author.

5.2.3.2 Simulation from empirical data

Now that the sphericity was measured, it is interesting to estimate how much of the frequency arrangement can be explained by the geometry.

One simulation was made using the "worst" scenario data, that is, using the maximum and minimum measured radii (323.03, 323.50 mm) as the semimajor and semiminor axis of the ellipsis, with the intermediate being the average (323.33 mm).

However, the results obtained were not reliable. As mentioned before, the choice of mesh parameters will have an effect on the exact value of the resonant frequencies. In this case, minor tweaking on the meshing, either increasing or decreasing the resolution, was enough to change the distribution of frequencies more than when changing the value of the radii up to the desired combination.

Therefore, although it seems safe to assume that due to the imperfections of the surface *some* variation is introduced in the way the frequencies are arranged, it is now possible to know how much, at least for now.

Figure 5.9 - Diagram of a spherometer.
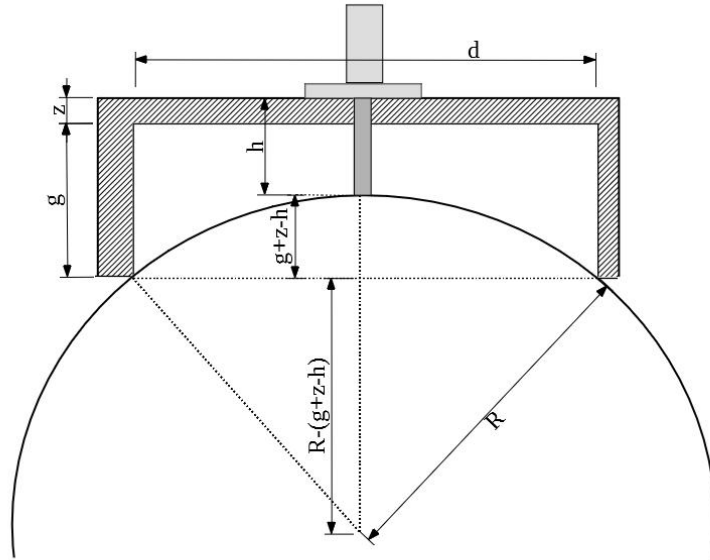
SOURCE: From the author.

5.3 Simulation of most correct model

Finally, in order to improve upon the values available in the literature, a new simulation was done using the values measured and presented in this chapter. Here, an antenna based on a sphere is considered, with radius 323.33 mm and density $\rho = (7.96 \pm .02)$g/cm^3. Young modulus and Poisson's ratio were unchanged. Results are in Table 5.3.

The simulation was repeated after adding the model for transducers. As shown in Table 5.7, 17 modes were found. The models were visually identified from the animations generated by SolidWorks. This visualization rendered a model with exaggerated deformation and color scale representing radial displacement. Since the scale of deformations of surface and the secondary oscillators varies greatly, given the mechanical advantage, some adjustment is required to provide an adequate level of detail. From those there are three groups of quadrupole modes $(3 \times (2 + 2 + 1))$ and 2 modes where the surface of the sphere was still and all R_1 and R_2 oscillated together. In one case, the membranes r_2 traveled along their respective transducers (in phase, $\phi = 0$) and in the other, the membranes flexed against the movement of

Table 5.4 - Readings of the micrometer for each position on the surface of the antenna. Arrow symbols are alignment of the spherometer in respect to the local cardinal directions on the surface (↕: NS, ↔: EW, and so on). Latitudes of the point can be Top ($\sim +10°$), Mid $\sim +52°$ and Bottom $\sim -45°$. Columns are the longitude.

h (mm)		0°	60°	120°	180°	240°	300°
Top	↗	18.58	18.58	18.55	18.55	18.58	18.56
	↘	18.58	18.56	18.55	18.58	18.53	18.56
Mid	↕	18.57	18.55	18.54	18.58	18.55	18.55
	↔	18.59	18.55	18.55	18.56	18.55	18.51
Bottom	↗	18.54	18.56	18.56	18.55	18.50	18.57
	↘	18.55	18.58	18.57	18.53	18.58	18.58

SOURCE: From the author.

Table 5.5 - Calculated radius of curvature for each position on the surface of the antenna. Arrow symbols are alignment of the spherometer in respect to the local cardinal directions on the surface (↕: NS, ↔: EW, and so on). Latitudes of the point can be Top ($\sim +10°$), Mid $\sim +52°$ and Bottom $\sim -45°$. Columns are the longitude.

R (mm)		0°	60°	120°	180°	240°	300°
Top	↗	323.45	323.45	323.29	323.29	323.45	323.34
	↘	323.45	323.34	323.29	323.45	323.19	323.34
Mid	↕	323.40	323.29	323.24	323.45	323.29	323.29
	↔	323.50	323.29	323.29	323.34	323.29	323.08
Bottom	↗	323.24	323.34	323.34	323.29	323.03	323.40
	↘	323.29	323.45	323.40	323.19	323.45	323.45

SOURCE: From the author.

the transducers (out of phase, $\phi = \pi$).

Table 5.6 - Frequencies of quadrupole modes of most accurate model of isolated quasi-sphere.

323.33mm sphere	mesh			Results 2004	
	fine	finer	finest		
$\oplus$	3177.4	3178.0	3179.7	3172.49	$\bigcirc^?$
$\oplus'$	3178.0	3179.4	3180.2	3183.0	$\bigcirc^?$
$\otimes$	3203.9	3202.5	3202.9	3213.62	$\bigcirc^?$
$\otimes'$	3204.4	3203.3	3203.2	3222.9	$\bigcirc^?$
$\odot$	3217.9	3219.3	3219.5	3240.0	$\bigcirc^?$

(Modes — row label on left spanning the symbol rows)

SOURCE: From the author.

Table 5.7 - Frequencies of quadrupole modes of most accurate model of quasi-sphere with transducers. Symbols denoted with $^?$ indicate that a some ambiguity was present in the identification of the mode. Symbols denoted with ^{R} indicate that the harmonics were aligned with a system of coordinates rotated in respect to the axis of the antenna. Modes were identified visually from the animations rendered by SolidWorks

$r_2(\phi = 0)$	3147.2
$\odot$	3155.3
$\oplus$	3161.9
$\otimes$	3177.0
$\oplus'$	3196.2
$\otimes'$	3202.1
$\oplus^?$	3213.4
$\oplus'^?$	3217.3
$\otimes^?$	3233.8
$\otimes'^?$	3237.5
$\odot$	3250.6
$r_2(\phi = \pi)$	3361.9
$\otimes^{R?}$	3367.7
$\odot^{R}$	3371.6
$\oplus^{R?}$	3376.1
$\otimes'^{R?}$	3381.4
$\oplus'^{R?}$	3385.0

SOURCE: From the author.

6 SENSITIVITY CURVE

Previous works have calculated the sensitivity curve for a TIGA arrangement based on a sphere with degenerate quadrupole mode and containing six transducers, all tuned to the frequency of the quadrupole. Merkowitz e Johnson (1995) considered the transducer as a single oscillator. Costa (2006) expanded upon the previous one by allowing transducers as a pair of coupled oscillators. Here, the quadrupole modes are no longer considered degenerate, but rather, each one can vibrate at a unique frequency. The introduction of this feature better reflects the reality of how oscillators interact with one another, thus might produce a more faithful picture of the frequencies arrangement and the behavior of the sensitivity curve. This allows the use of empirical data (AGUIAR et al., 2004) to fix the frequencies of the quadrupole modes.

6.1 Noises

In this section, a brief overview of the noises is given (COSTA, 2006). Thermal noise occurs due to the thermal kinetic energy that the detector has due to its temperature. The equipartition of energy dictates that the energy should be, on average, equally divided into every degree of freedom. This includes the mechanic vibration of the components of the instrument. Here k_b is the Boltzmann constant, T the temperature of the system, m_i mass of the element, Q_i its mechanical quality factor.

$$S_{\text{Thermal}} = 4k_b T \omega \frac{m_i}{Q_i} \quad \text{N}^2/\text{Hz} \tag{6.1}$$

The back action noise is a consequence of the electromagnetic coupling between the source of microwaves and the cavity of the transducers. It is dependent on the parameters of the pump, such as amplitude noise $S_{\text{am}} \sim -140\,\text{dBc/Hz}$, incident power P_{inc}^2, pump frequency ω_p (angular) or $_p$ (Hz), the cavity parameter $\text{d}f/\text{d}x$, quality factor Q_e.

$$S_{\text{BA}} = \frac{P_{\text{inc}}^2}{2\omega_p^2} \left(\frac{2Q_e}{f_p} \frac{\text{d}f}{\text{d}x} \right)^2 S_{\text{am}} \quad \text{N}^2/\text{Hz} \tag{6.2}$$

Similar to the previous case, the phase noise is also dependent on the characteristics of microwave source. This is a consequence of the pump not being perfectly monochromatic. The phase noise of the pump is $S_{\text{pph}} \sim -130\,\text{dBc/Hz}$.

$$S_{\text{phase}} = S_{\text{pph}} \left(\frac{2\pi}{\omega} \frac{\text{d}f}{\text{d}x} \right)^{-2} \quad \text{m}^2/\text{Hz} \tag{6.3}$$

Lastly, series noise arises during the amplification of the signal. It depends on the amplifier noise temperature T_{amp}.

$$S_{\text{series}} = L_{\text{amp}} \frac{(T_{\text{amp}} + T)k_b}{P_{\text{inc}}} \left(\frac{2Q_e}{f_p} \frac{df}{dx} \right)^{-2} \quad \text{m}^2/\text{Hz} \tag{6.4}$$

6.2   Model of the curve

From (3.52), the power spectral density $\underline{S}^g = \tilde{g}^2$ should be:

$$\underline{S}^g(\omega) = |\tilde{\underline{\xi}}(\omega)|^2 \underline{S}^{F_S}(\omega) + |\tilde{\underline{\Omega}}_1(\omega)|^2 \underline{S}^{F_1^N}(\omega) |\tilde{\underline{\Omega}}_2(\omega)|^2 \underline{S}^{F_2^N}(\omega) \tag{6.5}$$

So, considering Equation (3.56)

$$\tilde{\underline{h}}(\omega) = \left| \frac{2}{\omega^2 m_S \chi R} \underline{\underline{\xi}}^{-1}(\omega) \sqrt{S^g(\omega)} \right| \tag{6.6}$$

Now, it is needed to find a way to find a expression for the PSD. Using (3.34), rewrite it so the terms are

$$\underline{\underline{M}}' \ddot{\underline{x}} + \underline{\underline{C}}' \dot{\underline{x}} + \underline{\underline{K}}' \underline{x} = \underline{\underline{P}} \underline{f} \tag{6.7}$$

where

$$\underline{x} = \begin{pmatrix} \ddot{\underline{A}}(t) \\ \ddot{\underline{q}}_1(t) \\ \ddot{\underline{q}}_2(t) \end{pmatrix}; \qquad \underline{F} = \begin{pmatrix} \underline{F}_S(t) \\ \underline{F}_1^N(t) \\ \underline{F}_2^N(t) \end{pmatrix}; \qquad \underline{\underline{P}} = \begin{pmatrix} \underline{\underline{I}} & -\alpha \underline{\underline{B}} & \underline{\underline{0}} \\ \underline{\underline{0}} & \underline{\underline{I}} & -\underline{\underline{I}} \\ \underline{\underline{0}} & \underline{\underline{0}} & \underline{\underline{I}} \end{pmatrix} \tag{6.8}$$

Defining the ratios $\mu^2 = M_{R_1}/M_{\text{eff}}$, $\nu^2 = MS/M_{\text{eff}}$, it becomes:

$$\underline{\underline{M}}' = \begin{pmatrix} m_S \underline{\underline{I}} & \underline{\underline{0}} & \underline{\underline{0}} \\ m_{R_1} \alpha \underline{\underline{B}}^T & m_{R_1} \underline{\underline{I}} & \underline{\underline{0}} \\ m_{R_2} \alpha \underline{\underline{B}}^T & m_{R_2} \underline{\underline{I}} & m_{R_2} \underline{\underline{I}} \end{pmatrix}$$

$$\underline{\underline{M}}' = M_{\text{eff}} \begin{pmatrix} \nu^2 \underline{\underline{I}} & 0 & 0 \\ \mu^2 \alpha \underline{\underline{B}}^T & \mu^2 \underline{\underline{I}} & 0 \\ \mu^4 \alpha \underline{\underline{B}}^T & \mu^4 \underline{\underline{I}} & \mu^4 \underline{\underline{I}} \end{pmatrix} = M_{\text{eff}} \underline{\underline{M}} \tag{6.9}$$

Next, let's do the same for the matrix of elastic coefficients. Pay attention that, difference from previous model, now $\underline{k_S}$ comprises of multiple values

$$\underline{\underline{K}}' = \begin{pmatrix} \mathrm{diag}(\underline{k_S}) & -k_{R_1}\alpha\underline{\underline{B}} & \underline{\underline{0}} \\ \underline{\underline{0}} & k_{R_1}\underline{\underline{I}} & -k_{R_2}\underline{\underline{I}} \\ \underline{\underline{0}} & \underline{\underline{0}} & k_{R_2}\underline{\underline{I}} \end{pmatrix}$$

$$\underline{\underline{K}}' = M_{\mathrm{eff}}\omega_0^2 \begin{pmatrix} \nu^2\mathrm{diag}\left(\frac{\omega_n^2}{\omega_0^2}\right) & -\mu^2\alpha\underline{\underline{B}} & \underline{\underline{0}} \\ \underline{\underline{0}} & \mu^2\underline{\underline{I}} & -\mu^4\underline{\underline{I}} \\ \underline{\underline{0}} & \underline{\underline{0}} & \mu^4\underline{\underline{I}} \end{pmatrix} = M_{\mathrm{eff}}\omega_0^2\underline{\underline{K}} \tag{6.10}$$

And to the the dampening coefficients

$$\underline{\underline{C}}' = \begin{pmatrix} \mathrm{diag}(\underline{H_S}) & -H_{R_1}\alpha\underline{\underline{B}} & \underline{\underline{0}} \\ \underline{\underline{0}} & H_{R_1}\underline{\underline{I}} & -H_{R_2}\underline{\underline{I}} \\ \underline{\underline{0}} & \underline{\underline{0}} & H_{R_2}\underline{\underline{I}} \end{pmatrix}$$

$$\underline{\underline{C}}' = M_{\mathrm{eff}}\frac{\omega_0}{Q} \begin{pmatrix} \nu^2\mathrm{diag}\left(\frac{\omega_n}{\omega_0}\right) & -\mu^2\frac{Q}{Q_{R_1}}\alpha\underline{\underline{B}} & \underline{\underline{B}} \\ \underline{\underline{0}} & \mu^2\frac{Q}{Q_{R_1}}\underline{\underline{I}} & -\mu^4\frac{Q}{Q_{R_2}}\underline{\underline{I}} \\ \underline{\underline{0}} & \underline{\underline{0}} & \mu^4\frac{Q}{Q_{R_2}}\underline{\underline{I}} \end{pmatrix} = M_{\mathrm{eff}}\frac{\omega_0}{Q}\underline{\underline{C}} \tag{6.11}$$

Therefore, the movement equations can be rewritten as

$$M_{\mathrm{eff}}\underline{\underline{M}}\ddot{\underline{x}} + M_{\mathrm{eff}}\frac{\omega_0}{Q}\underline{\underline{C}}\dot{\underline{x}} + M_{\mathrm{eff}}\omega_0^2\underline{\underline{K}}\underline{x} = \underline{\underline{P}}\underline{F}(t) \tag{6.12}$$

To proceed, let's define the matrix $\underline{\underline{N}}$

$$\underline{\underline{N}} = \begin{pmatrix} \underline{\underline{I}}/\nu & \underline{\underline{0}} & \underline{\underline{0}} \\ \underline{\underline{0}} & \underline{\underline{I}}/\mu & \underline{\underline{0}} \\ \underline{\underline{0}} & \underline{\underline{0}} & \underline{\underline{I}}/\mu^2 \end{pmatrix} \tag{6.13}$$

Using it, define new matrices

$$\underline{\underline{C}}_y = (\underline{\underline{N}}\underline{\underline{M}}\underline{\underline{N}})^{-1}\underline{\underline{N}}\underline{\underline{C}}\underline{\underline{N}} \tag{6.14a}$$

$$\underline{\underline{K}}_y = (\underline{\underline{N}}\underline{\underline{M}}\underline{\underline{N}})^{-1}\underline{\underline{N}}\underline{\underline{K}}\underline{\underline{N}} \tag{6.14b}$$

$$\underline{\underline{P}}_y = (\underline{\underline{N}}\underline{\underline{M}}\underline{\underline{N}})^{-1}\underline{\underline{N}}\underline{\underline{P}} \tag{6.14c}$$

With a change of coordinates $\underline{x} = \underline{\underline{N}}\underline{y}$, the system of equations will be rewritten in

a diagonal form:

$$M_{\text{eff}}\underline{\underline{NMN}}\ddot{y} + M_{\text{eff}}\frac{\omega_0}{Q}\underline{\underline{NCN}}\dot{y} + M_{\text{eff}}\omega_0^2\underline{\underline{NKN}}y = \underline{\underline{NP}}f \tag{6.15}$$

Now, substituting the matrices (6.14)

$$M_{\text{eff}}\ddot{y} + 2\beta M_{\text{eff}}\underline{\underline{M}}_y^{-1}\underline{\underline{C}}_y\underline{y} + M_{\text{eff}}\omega_0^2\underline{\underline{M}}_y^{-1}\underline{\underline{K}}_y\underline{y} = \underline{\underline{M}}_y^{-1}\underline{\underline{P}}_y f \tag{6.16}$$

Denoting $\underline{\underline{C}}_z = \underline{\underline{M}}_y^{-1}\underline{\underline{C}}_y$, $\underline{\underline{K}}_z = \underline{\underline{M}}_y^{-1}\underline{\underline{K}}_y$ and $\underline{\underline{P}}_z = \underline{\underline{M}}_y^{-1}\underline{\underline{P}}_y$, the equations will be

$$M_{\text{eff}}\ddot{y} + 2\beta M_{\text{eff}}\underline{\underline{C}}_z\underline{y} + M_{\text{eff}}\omega_0^2\underline{\underline{K}}_z\underline{y} = \underline{\underline{P}}_z f \tag{6.17}$$

now with the use of a modal matrix U and some algebraic manipulations, we can diagonalize this matrix:

$$M_{\text{eff}}\underline{\underline{U}}^{-1}\ddot{y} + 2\beta M_{\text{eff}}\underline{\underline{U}}^{-1}\underline{\underline{C}}_z\underline{\underline{U}}\,\underline{\underline{U}}^{-1}\dot{y} + M_{\text{eff}}\omega_0^2\underline{\underline{U}}^{-1}\underline{\underline{K}}_z\underline{\underline{U}}\,\underline{\underline{U}}^{-1}y = \underline{\underline{U}}^{-1}\underline{\underline{P}}_z f \tag{6.18}$$

with another change of coordinates $\underline{z} = \underline{\underline{U}}^{-1}\underline{y}$, define the diagonal matrix $\underline{\underline{D}} = \underline{\underline{U}}^{-1}\underline{\underline{K}}_z\underline{\underline{U}}$ and take the Fourier transform

$$(-M_{\text{eff}}\omega^2\underline{\underline{I}} + 2j\beta M_{\text{eff}}\omega\underline{\underline{U}}^{-1}\underline{\underline{C}}_z\underline{\underline{U}} + M_{\text{eff}}\omega_0^2\underline{\underline{D}})\tilde{z} = \underline{\underline{U}}^{-1}\underline{\underline{P}}_z f \tag{6.19}$$

the matrix $\underline{\underline{D}}$

$$\underline{\underline{D}} = \underline{\underline{U}}^{-1}\underline{\underline{K}}_z\underline{\underline{U}} \tag{6.20}$$

Contains the eigenvalues from the matrix of the elastic coefficients. From these values, the values of the frequencies of the resonant modes can be computed.

$$f_n = \frac{\omega_n}{2\pi} \tag{6.21}$$

These values are presented in Table 6.1.

However, the matrix of the dampening coefficients $\underline{\underline{U}}^{-1}\underline{\underline{C}}_z\underline{\underline{U}}$ is not diagonal. And not much more can be done with this approach.

So instead, there is another way to proceed. The response for each frequency can be computed. To do this, we get back to the equations of motion

$$M_{\text{eff}}(-\omega^2\underline{\underline{M}} + 2\beta j\omega\underline{\underline{C}} + \omega_0^2\underline{\underline{K}})\underline{x} = \underline{\underline{P}}F(\omega) \tag{6.22}$$

Table 6.1 - Resonant frequencies of the system, in Hz, as given by the eigenvalues of the diagonalized equation of motion and the valleys of the computed sensitivity curves. The backaction column is singled out to emphasize its singular frequency arrangement.

From eigenvalues	From noise curves				
	Thermal	Phase	Serie	Total	Backa
3158.8	3158.7	3158.7	3158.7	3158.7	3161.6
3165.2	3165.0	3165.0	3165.0	3165.0	3169.7
3175.2	3175.1	3175.1	3175.1	3175.1	3187.6
3176.6	3176.4	3176.4	3176.4	3176.4	3187.9
3178.1	3178.0	3178.0	3178.0	3178.0	3191.0
3182.3	-	-			3191.4
3191.8	3191.8	3191.8	3191.8	3191.8	3195.3
3195.1	3195.1	3195.1	3195.1	3195.1	3195.8
3210.5	3210.5	3210.5	3210.5	3210.5	3216.8
3215.2	3215.2	3215.2	3215.2	3215.2	3217.4
3221.6	3221.5	3221.5	3221.5	3221.5	3219.2
3231.3	-	-			3219.7
3235.4	3235.2	3235.2	3235.2	3235.2	3232.0
3236.2	3236.0	3236.0	3236.0	3236.0	3237.9
3241.3	3241.1	3241.1	3241.1	3241.1	3250.6
3244.5	3244.4	3244.4	3244.4	3244.4	
3253.7	3253.7	3253.7	3253.7	3253.7	

SOURCE: From the author.

And define $\underline{\underline{L}}$ so

$$\underline{\underline{L}}(\omega)\underline{x} = \underline{\underline{P}}\underline{F}(\omega) \tag{6.23}$$

therefore

$$\underline{x} = \underline{\underline{L}}^{-1}\underline{\underline{P}}\underline{F} \tag{6.24}$$

In this manner, a relation of F and x is achieved:

$$\underline{x} = \underline{\underline{H}}(\omega)\underline{F} \tag{6.25}$$

Remember that we are most interested in the terms of q_2 and F_S, so, writing in an

explicit form:

$$x = \begin{pmatrix} \tilde{\underline{A}} \\ \tilde{\underline{q}}_1 \\ \tilde{\underline{q}}_2 \end{pmatrix} = \begin{pmatrix} \underline{\underline{H}}_{11} & \underline{\underline{H}}_{12} & \underline{\underline{H}}_{13} \\ \underline{\underline{H}}_{21} & \underline{\underline{H}}_{22} & \underline{\underline{H}}_{23} \\ \underline{\underline{H}}_{31} & \underline{\underline{H}}_{32} & \underline{\underline{H}}_{33} \end{pmatrix} \begin{pmatrix} \tilde{\underline{F}}_S \\ \tilde{\underline{F}}_1^N \\ \tilde{\underline{F}}_2^N \end{pmatrix} \tag{6.26}$$

They are combined in the expression:

$$\tilde{\underline{q}}_2 = \underline{\underline{H}}_{31} \tilde{\underline{F}}_S \tag{6.27}$$

Using the definition from Equation (3.23)

$$\tilde{\underline{q}}_2 = -\frac{1}{2} M_S \chi R \omega^2 \underline{\underline{H}}_{31} \tilde{\underline{h}}_m \tag{6.28}$$

using the matrix defined in (A.3), we arrive at a expression in terms of h in the frame of the detector

$$\tilde{\underline{q}}_2 = -\frac{1}{2} M_S \chi R \omega^2 \underline{\underline{H}}_{31} \underline{\underline{T}}_V \tilde{\underline{h}} \tag{6.29}$$

Let's consider the expression for the signal to noise ratio (SNR) for a matched filter that considers a signal h (USENKO, 2012)

$$\rho^2 = \frac{1}{2\pi} \int \tilde{\underline{q}}_{R_2}^{GWH} \underline{\underline{S}}_{R_2 R_2}^{-1} \tilde{\underline{q}}_{R_2}^{GW} \, d\omega \tag{6.30}$$

The fluctuation dissipation theorem stays that, for a body with a temperature T, the spectral density of the Brownian noise of a resonator is

$$\underline{\underline{S}}_{xx} = \frac{4 k_B T}{\omega^2} \text{Re}(\underline{Y}(\omega)) \tag{6.31}$$

We define the sensitivity curve of detector as the equivalent signal h that would be equal to the output produced by thermal noise, that is, a SNR $\rho = 1$. Therefore

$$\tilde{\underline{q}}_{R_2}^{GWH} \underline{\underline{R}}_{33} \tilde{\underline{q}}_{R_2}^{GW} = 1 \tag{6.32}$$

where $\underline{\underline{R}} = \underline{\underline{S}}_{xx}^{-1}$. Here I'll only be using adding the thermal noise. Adding the other noise components will make harder to distinguish the frequencies' arrangement, which would be counterproductive to this work. So the results presented from now on will be an best case scenario, with ideal, noiseless, amplifiers and pump. Substituting the definition from Equation (6.29):

$$\left(-\frac{1}{2} M_S \chi R \omega^2 \right)^2 \underline{\underline{H}}_{31}{}^H \underline{\underline{T}}_V^H \tilde{\underline{h}}^H \underline{\underline{R}}_{33} \underline{\underline{H}}_{31} \underline{\underline{T}}_V \tilde{\underline{h}} = 1 \tag{6.33}$$

Now we write this equation in terms of the input variables. There is freedom to add an angles ϕ in the frame of the observer, that allows the simplification of the polarization terms, so $h'_\times = 0$ and $h'_+ = \sqrt{h_+^2 + h_\times^2}$. The non-zero terms that will contribute to h_S are

$$h_S(w) = \frac{1}{\left(\frac{1}{2}M_S\chi Rw^2\right)\sqrt{(\underline{\underline{T_v}}^H \underline{\underline{H}}_{31}^H \underline{\underline{R}}_{33} \underline{\underline{H}}_{31} \underline{\underline{T_v}})_{11}}} \tag{6.34}$$

If we now define

$$\underline{\underline{A}} = \underline{\underline{H}}_{31}^H \underline{\underline{R}}_{33} \underline{\underline{H}}_{31} \tag{6.35}$$

averaging across all directions If we take the mean value of all directions of incoming GW we obtain

$$\overline{\underline{\underline{T_v^H A T_v}}} = \text{Tr}\left(\underline{\underline{A}}\right) \tag{6.36}$$

That will be substituted in the previous equation so

$$\left(-\frac{1}{2}M_S\chi Rw^2\right)^2 h_S(w)^2 \left(A_{11} + A_{22} + A_{33} + A_{44} + A_{55}\right) = 1 \tag{6.37}$$

Thus

$$h_S(w) = \frac{1}{\left(\frac{1}{2}M_S\chi Rw^2\right)\sqrt{A_{11} + A_{22} + A_{33} + A_{44} + A_{55}}} \tag{6.38}$$

Which is finally a way to compute the curve of strain sensitivity for a given spectrum. The parameters used in the simulations are written in Table 6.2.

Evaluating the expression, each time considering only one of the noises and then once with all their contributions. Their respective sensitivity curve are presented in Figure 6.1. The curve indicates a working region around $\sim 10^{-19}/\sqrt{\text{Hz}}$ between 3160 and $3260Hz$. A function to find the peaks was employed and 15 peaks were detected in each curve. The values of their frequencies are presented in Table 6.1.

The dominating noise is the series noise, which almost corresponds to the total designed sensitivity curve. The thermal, phase and backaction noises follow, each with a decreasing contribution to the overall curve.

Comparing these frequencies obtained by the ones calculated by eigenvalues, they match exactly for most of the curves. The backaction curve has a singular frequency arrangement. For the remaining ones, the two values found only on the eigenvalues column (3182.3 and 3231.3) do not have the slightest in indication in their curves. It is not yet known with certainty what this could be, but perhaps they could be the modes that produce no excitation on the surface of the sphere. In the simulation

Table 6.2 - Simulation parameters.

Symbol	value	parameter
R	$0.323\,\text{m}$	radius of sphere
M_S	$1124\,\text{kg}$	mass of sphere
ρ	$7960\,\text{kg/m}^3$	density of sphere
f_{0n}	$(3172.5,\ 3183.0,$	measured natural
	$3213.6,\ 3222.9,\ 3240.0)\,\text{Hz}$	frequencies
Q	10^6	mechanical quality factor
T	$4.2\,\text{K}$	sphere temperature
M_{eff}	$281\,\text{kg}$	effective mass
M_{R2}	$0.0000123\,\text{kg}$	mass of second resonator
M_{R1}	$\sqrt{M_{\text{eff}}M_{R2}}\,\text{kg}$	mass of first resonator
ω_{R1}	$3206.3\,\text{Hz}$	natural frequency of first resonator
ω_{R2}	$3206.3\,\text{Hz}$	natural frequency of second resonator
Q_{R1}	10^5	quality factor of first resonator
Q_{R2}	10^4	quality factor of second resonator
F_{3T}	$3206.3\,\text{Hz}$	transducer frequency
F_{pump}	$10^9\,\text{Hz}$	pump frequency
β_e	0.3	electric coupling factor
$\mathrm{d}f/\mathrm{d}x$	$7.26{\times}10^{14}$	membrane frequency shift response
P_{inc}	$5{\times}10^{-11}\,\text{W}$	incident power
T_{amp}	$8\,\text{K}$	amplifier noise temperature
Q_e	$3{\times}10^5$	electrical quality factor
S_{pm}	10^{-13}	phase noise spectral density
S_{am}	10^{-14}	amplifier noise spectral density
L_{amp}	0.5	transducer-amplifier inverse coupling

SOURCE: From the author.

referenced in Table 5.3 two of these were also detected.

Figure 6.1 - Schenberg designed sensitivity curve

.
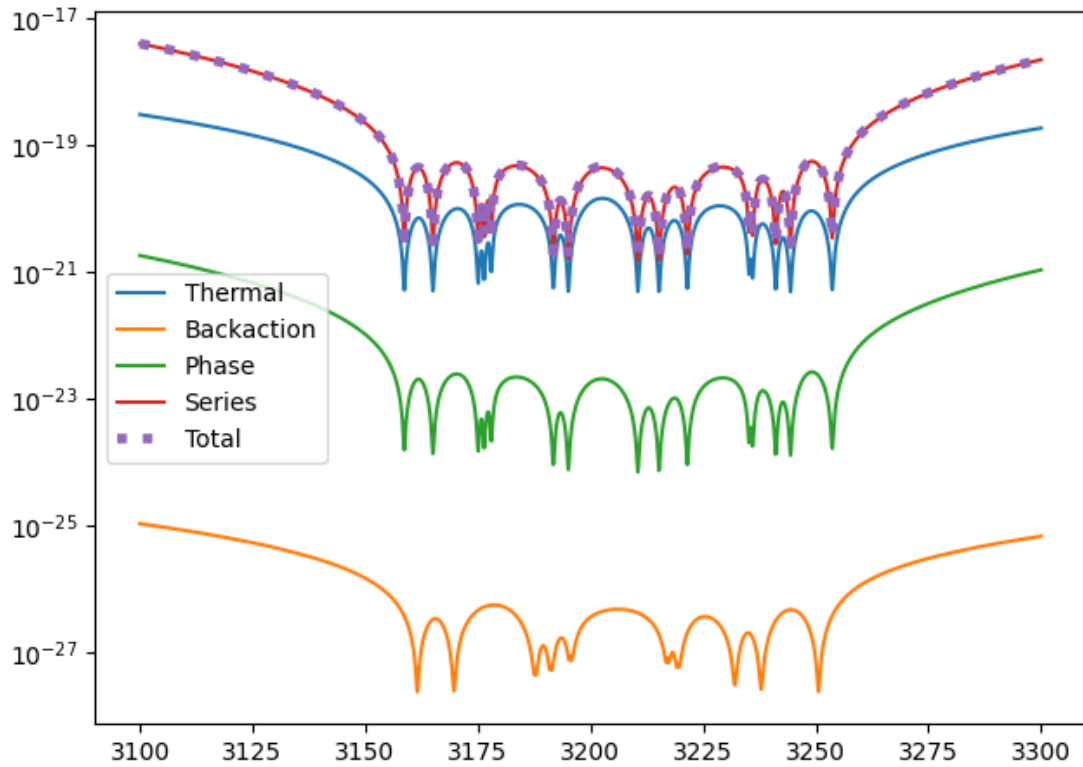
In conclusion, this new sensitivity curve shows features expected from the model that includes a non-degenerate group of quadrupole modes, and is possibly a more complete representation of the capabilities of the detector.

7 CONCLUSIONS

In this work, progress was made in understanding how the quadrupole resonant frequencies of the resonant mass depends on the properties of the mass distribution of the body. This could provide an explanation, at least partial, for the measured frequency arrangement of the Schenberg antenna. However, some ideas were not yet considered, as for example, how the suspension couples with the quadrupole modes. And, of course, there could be unknown unknowns that also could cause the observed behavior.

To either confirm of discard this hypothesis, an experimental setup capable of measuring the moments of the mass distribution would be required, perhaps with an apparatus capable of rotating the antenna around any axis and registering the torque, or pointing the position of the center of mass using statics. Both are not trivial given the mass and of the body.

Additionally, the need for a more refined FEM simulation is justified. The measurements of the radius of curvature shows an overall roundness of the body, but the deviation from a perfect sphere should account for some of the splitting of the degenerate pair of frequencies. Ideally, a high-resolution model would be reconstructed from 3D measurements of the surface of the body. And metallurgical analysis from samples could show how heterogeneous is the material and whether the simulation should allow for variation of its mechanical properties. Overall, there's the recommendation for a commissioning that allows greater accountability, with verification and validation steps all along the way.

In regard to the sensitivity curve, the revamped model is more in tune with the physical reality of the frequencies' arrangement, as it is now allowing non-degenerate modes of the sphere. There is still space for improvement, as this model was not derived from first principles but uses empirical data to describe the frequencies of resonance. An avenue for improvement would be to use FEM to calculate the frequencies from the high resolution measured geometry. With the same data we could determine the effective mass of each mode, instead of using the one value calculated for the degenerate modes of a sphere.

Finally, here are a set of recommendations for future resonant mass detectors. For a tighter control on the sensitivity curve, one of the aspects of the project should be the specification of the tolerances on the geometry of the body and mechanical properties of the material. Additionally, care should be taken during commissioning

to characterize and validate the model used to calculate the frequency arrangement. Also, it was learned that perhaps it is feasible to fine tune the quadrupole frequencies, and maybe this could be exploited to locate the resonant modes in order to either widen the band or deepen the sensitivity curve.

REFERENCES

ABBOTT, B. P.; ABBOTT, R.; ABBOTT, T. D.; ABERNATHY, M. R. Observation of gravitational waves from a binary black hole merger. **Physical Review Letters**, v. 116, p. 061102, Feb 2016. 1

AGUIAR, O.; ANDRADE, L.; CAMARGO FILHO, L.; COSTA, C.; ARAUJO, J. d.; REY NETO, E. d.; SOUZA, S. d.; FAUTH, A.; FRAJUCA, C.; FROSSATI, G.; FURTADO, S.; FURTADO, V.; AES, N. M.; MARINHO JUNIOR, R.; MATOS, E.; MELIANI, M.; MELO, J.; MIRANDA, O.; OLIVEIRA JUNIOR, N.; RIBEIRO, K.; SALLES, K.; STELLATI, C.; VELLOSO JUNIOR, W. The gravitational wave detector "Mario Schenberg": status of the project. **Brazilian Journal of Physics**, v. 32, p. 866–868, 12 2002. 1

AGUIAR, O. D.; ANDRADE, L. A.; BARROSO, J. J.; CAMARGO FILHO, L.; CARNEIRO, L. A.; CASTRO, C. S.; CASTRO, P. J.; COSTA, C. A.; COSTA, K. M. F.; ARAUJO, J. C. N. de; LUCENA, A. U. de; PAULA, W. de; REY NETO, E. C. de; SOUZA, S. T. de; FAUTH, A. C.; FRAJUCA, C.; FROSSATI, G.; FURTADO, S. R.; LIMA, L. C.; MAGALHÃES, N. S.; MARINHO, R. M.; MATOS, E. S.; MELO, J. L.; MIRANDA, O. D.; OLIVEIRA, N. F.; PALEO, B. W.; REMY, M.; RIBEIRO, K. L.; STELLATI, C.; VELLOSO, W. F.; WEBER, J. The brazilian spherical detector: progress and plans. **Classical and Quantum Gravity**, v. 21, n. 5, p. S457–S463, feb 2004. 1, 29, 31, 45, 55

AGUIAR, O. D. et al. The Schenberg spherical gravitational wave detector: the first commissioning runs. **Classical and Quantum Gravity**, v. 25, n. 11, p. 114042, may 2008. 1, 35, 37

_____. Status report of the Schenberg gravitational wave antenna. **Journal of Physics: Conference Series**, v. 363, p. 012003, jun 2012. 1

AGUIAR, O. D. de. **Future prospects of Schenberg**. March 2021. Personal communications. 1

ALBERT, A. et al. Search for multimessenger sources of gravitational waves and high-energy neutrinos with advanced LIGO during its first observing run, ANTARES, and IceCube. **The Astrophysical Journal**, v. 870, n. 2, p. 134, jan 2019. Disponível em: <https://doi.org/10.3847/1538-4357/aaf21d>. 1

ANDRADE, L. A.; COSTA, C. A.; AGUIAR, O. D.; FRAJUCA, C.; MOSSO, M. M.; PODCAMENI, A.; SILVA, H. J. P. P. da; MAGALHÃES, N. S. Ultra-low

phase noise 10 GHz oscillator to pump the parametric transducers of the Mario Schenberg gravitational wave detector. **Classical and Quantum Gravity**, v. 21, n. 5, p. S1215–S1219, feb 2004. 35

ANDRADE, L. A. de. **Cálculo do ruído de uma antena esférica para ondas gravitacionais acoplada a transdutores paramétricos**. Thesis (Master in Astrophysics) — Instituto Nacional de Pesquisas Espaciais, São José dos Campos, 2001. 35, 40

ASHBY, N.; DREITLEIN, J. Gravitational wave reception by a sphere. **Physical Review D**, v. 12, p. 336–349, Jul 1975. Disponível em: <https://link.aps.org/doi/10.1103/PhysRevD.12.336>. 13

BORTOLI, F. d. S. **Sistemas vibracionais do detector de ondas gravitacionais Mario Schenberg**. Thesis (PhD in Physics) — Universidade de São Paulo, São Paulo, 2011. 30, 31, 32, 34, 35, 39, 40, 42, 45

BORTOLI, F. S.; FRAJUCA, C.; MAGALHAES, N. S. A method to design mechanical transducers for resonant-mass gravitational wave detectors. **Astronomische Nachrichten**, v. 342, n. 1-2, p. 123–127, 2021. Disponível em: <https://onlinelibrary.wiley.com/doi/abs/10.1002/asna.202113891>. 30

BUIKEMA, A. et al. Sensitivity and performance of the advanced ligo detectors in the third observing run. **Physical Review D**, v. 102, p. 062003, Sep 2020. Disponível em: <https://link.aps.org/doi/10.1103/PhysRevD.102.062003>. 1

CALLISTER, W.; RETHWISCH, D. **Materials science and engineering**. [S.l.: s.n.], 2014. ISBN 9781118319222. 38

CAMPBELL, J. **Complete casting handbook**. 2. ed. Boston: [s.n.], 2015. ISBN 978-0-444-63509-9. 38

CERVANTES-COTA, J.; GALINDO-URIBARRI, S.; SMOOT, G. A brief history of gravitational waves. **Universe**, v. 2, n. 3, p. 22, Sept. 2016. ISSN 2218-1997. Disponível em: <http://dx.doi.org/10.3390/universe2030022>. 5

COSTA, C. **Simulação da resposta do detector Mario Schenberg a ondas gravitacionais oriundas de fontes astrofísicas**. Thesis (PhD in Astrophysics) — Instituto Nacional de Pesquisas Espaciais, São José dos Campos, 2006. 22, 35, 55

FERREIRA, P. G. Cosmological tests of gravity. **Annual Review of Astronomy and Astrophysics**, v. 57, n. 1, p. 335–374, 2019. 1

FRAJUCA, C.; RIBEIRO, K. L.; ANDRADE, L. A.; AGUIAR, O. D.; MAGALHÃES, N. S.; MARINHO, R. de M. A noise model for the brazilian gravitational wave detector Mario Schenberg. **Classical and Quantum Gravity**, v. 21, n. 5, p. S1107–S1111, feb 2004. 35

GOLDSTEIN, H. **Classical mechanics**. [S.l.: s.n.], 1980. 20

GOTTARDI, L.; WAARD, A. de; USENKO, O.; FROSSATI, G.; PODT, M.; FLOKSTRA, J.; BASSAN, M.; FAFONE, V.; MINENKOV, Y.; ROCCHI, A. Sensitivity of the spherical gravitational wave detector minigrail operating at 5 k. **Physical Review D**, v. 76, p. 102005, Nov 2007. Disponível em: <https://link.aps.org/doi/10.1103/PhysRevD.76.102005>. 35

HARMS, J. et al. Lunar gravitational-wave antenna. **The Astrophysical Journal**, v. 910, n. 1, p. 1, mar 2021. Disponível em: <https://doi.org/10.3847/1538-4357/abe5a7>. 2

HULSE, R. A.; TAYLOR, J. H. Discovery of a pulsar in a binary system. **Astrophysical Journal**, v. 195, p. L51–L53, jan. 1975. 15

JACKSON, J. D. **Classical electrodynamics**. 3. ed. New York, NY: [s.n.], 1999. 9, 10, 30

JOHNSON, W. W.; MERKOWITZ, S. M. Truncated icosahedral gravitational wave antenna. **Physical Review Letters**, v. 70, p. 2367–2370, Apr 1993. 22

LANDAU, E. M. L. L. D. **Theory of elasticity**. 2. ed. [s.n.], 1981. (Course of Theoretical Physics, Volume 7). ISBN 9780080064659,9780750626330,0080064655,075062633X. Disponível em: <http://gen.lib.rus.ec/book/index.php?md5=16AF3489BECF3EA6FB1D585B40658FCD>. 15, 30

LOBO, J. A. What can we learn about gravitational wave physics with an elastic spherical antenna? **Physical Review D**, v. 52, p. 591–604, Jul 1995. Disponível em: <https://link.aps.org/doi/10.1103/PhysRevD.52.591>. 26

MAGGIORE, M. **Gravitational waves: volume 1: theory and experiments**. [S.l.: s.n.], 2008. (Gravitational Waves). ISBN 9780198570745. 5, 7, 9, 10

MERKOWITZ, S. M. **Truncated icosahedral gravitational wave antenna**. Thesis (PhD in Physics), Disponível em https://digitalcommons.lsu.edu/gradschool_disstheses/6033 — Louisiana State University, Baton Rouge, 1995. 13, 17, 20

MERKOWITZ, S. M.; JOHNSON, W. W. Spherical gravitational wave antennas and the truncated icosahedral arrangement. **Physical Review D**, v. 51, p. 2546–2558, Mar 1995. Disponível em: <https://link.aps.org/doi/10.1103/PhysRevD.51.2546>. 16, 27, 35, 55

_____. Techniques for detecting gravitational waves with a spherical antenna. **Physical Review D**, v. 56, p. 7513–7528, Dec 1997. Disponível em: <https://link.aps.org/doi/10.1103/PhysRevD.56.7513>. 26, 35

MISNER, C. W.; THORNE, K. S.; WHEELER, J. A. **Gravitation**. San Francisco: W. H. Freeman, 1973. ISBN 978-0-7167-0344-0, 978-0-691-17779-3. 11

OLIVEIRA, N. F.; AGUIAR, O. D. The Mario Schenberg gravitational wave antenna. **Brazilian Journal of Physics**, v. 46, p. 596–603, 2016. 1

SCHICKORE, J. Scientific discovery. In: ZALTA, E. N. (Ed.). **The Stanford encyclopedia of philosophy**. Summer 2018. [S.l.: s.n.], 2018. 2

TOBAR, M.; IVANOV, E.; BLAIR, D. Parametric transducers for the advanced cryogenic resonant-mass gravitational wave detectors. **General Relativity and Gravitation**, v. 32, p. 1799 – 1821, 2000. 1

USENKO, O. **Development and testing of the gravitational wave antenna MiniGRAIL in its full-featured configuration**. Thesis (PhD in Physics) — Leiden University, Leiden, 2012. 60

WEBER, J. Detection and generation of gravitational waves. **Physical Review**, v. 117, p. 306–313, Jan 1960. 15

Wikimedia Commons. **Truncated icosahedron**. 2005. File: Truncatedicosahedron.jpg. Disponível em: <https://en.wikipedia.org/wiki/File:Truncatedicosahedron.jpg>. 27

ANNEX A TABLES OF SPHERICAL HARMONICS AND DETECTOR MATRIX

$$Y_{2-2}(\theta, \varphi) = \frac{1}{4}\sqrt{\frac{15}{2\pi}} \cdot e^{-2i\varphi} \cdot \sin^2\theta \tag{A.1a}$$

$$Y_{2-1}(\theta, \varphi) = \frac{1}{2}\sqrt{\frac{15}{2\pi}} \cdot e^{-i\varphi} \cdot \sin\theta \cdot \cos\theta \tag{A.1b}$$

$$Y_{20}(\theta, \varphi) = \frac{1}{4}\sqrt{\frac{5}{\pi}} \cdot (3\cos^2\theta - 1) \tag{A.1c}$$

$$Y_{21}(\theta, \varphi) = -\frac{1}{2}\sqrt{\frac{15}{2\pi}} \cdot e^{i\varphi} \cdot \sin\theta \cdot \cos\theta \tag{A.1d}$$

$$Y_{22}(\theta, \varphi) = \frac{1}{4}\sqrt{\frac{15}{2\pi}} \cdot e^{2i\varphi} \cdot \sin^2\theta \tag{A.1e}$$

$$Y_1 = \sqrt{\frac{1}{2}}(Y_{22} + Y_{2-2}) \tag{A.2a}$$

$$Y_2 = \sqrt{\frac{1}{2}}i(Y_{2-2} - Y_{22}) \tag{A.2b}$$

$$Y_3 = \sqrt{\frac{1}{2}}i(Y_{21} + Y_{2-1}) \tag{A.2c}$$

$$Y_4 = \sqrt{\frac{1}{2}}(Y_{2-1} - Y_{21}) \tag{A.2d}$$

$$Y_5 = Y_{20} \tag{A.2e}$$

$$\underline{\underline{T_v}} = \sqrt{2} \begin{pmatrix} \frac{1}{2}(1+\cos^2\theta)\cos 2\phi & -\cos\theta\sin 2\phi \\ \frac{1}{2}(1+\cos^2\theta)\sin 2\phi & \cos\theta\cos 2\phi \\ -\frac{1}{2}\sin 2\theta\cos\phi & \sin\theta\sin\phi \\ -\frac{1}{2}\sin 2\theta\sin\phi & -\sin\theta\cos\phi \\ \frac{\sqrt{3}}{2}\sin^2\theta & 0 \end{pmatrix} \begin{pmatrix} \cos 2\psi & \sin 2\psi \\ -\sin 2\psi & \cos 2\psi \end{pmatrix} \tag{A.3}$$